

UniSTOK: Uniform Inductive Spatio-Temporal Kriging

Lewei Xie*
72404204@cityu-dg.edu.cn
City University of Hong Kong
(Dongguan)
Dongguan, China

Haoyu Zhang*
hzhang2838-c@my.cityu.edu.hk
City University of Hong Kong
Hong Kong, China

Juan Yuan†
yuanjuan0704@ruc.edu.cn
Renmin University of China
Beijing, China

Liangjun You‡
72540091@cityu-dg.edu.cn
City University of Hong Kong
(Dongguan)
Dongguan, China

Yulong Chen§
72405526@cityu-dg.edu.cn
City University of Hong Kong
(Dongguan)
Dongguan, China

Yifan Zhang¶
yif.zhang@cityu-dg.edu.cn
City University of Hong Kong
(Dongguan)
Dongguan, China

Abstract

Spatio-temporal kriging aims to infer signals at unobserved locations from observed sensors and is critical to applications such as transportation and environmental monitoring. In practice, however, observed sensors themselves often exhibit heterogeneous missingness, forcing inductive kriging models to rely on crudely imputed inputs. This setting brings three key challenges: (1) it is unclear whether an value is a true signal or a missingness-induced artifact; (2) missingness is highly heterogeneous across sensors and time; (3) missing observations distort the local spatio-temporal structure. To address these issues, we propose Uniform Inductive Spatio-Temporal Kriging (UniSTOK), a plug-and-play framework that enhances existing inductive kriging backbones under missing observation. Our framework forms a dual-branch input consisting of the original observations and a jigsaw-augmented counterpart that synthesizes proxy signals only at missing entries. The two branches are then processed in parallel by a shared spatio-temporal backbone with explicit missingness mask modulation. Their outputs are finally adaptively fused via dual-channel attention. Experiments on multiple real-world datasets under diverse missing patterns demonstrate consistent and significant improvements.

CCS Concepts

• **Computing methodologies** → **Neural networks.**

Keywords

Spatio-temporal Kriging, Graph Neural Networks, Missingness

1 Introduction

In spatio-temporal tasks, the deployment of sensors is fundamental, as they provide the raw observations that underpin downstream applications such as intelligent transportation [27, 28], environmental monitoring [7], and urban analytics [11, 12]. Ideally, sensor networks would densely cover the target region, enabling fine-grained modeling and decision making. In practice, however, the capital and maintenance costs of large-scale deployments [32] make it infeasible to instrument every location with sensors.

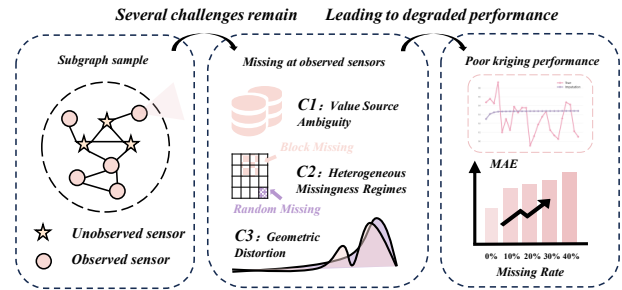


Figure 1: A introduction for ISK under observed missing.

With the recent development of Graph Neural Networks (GNNs) [14], inductive spatio-temporal kriging (ISK) [1, 35] has been proposed as a promising paradigm for this task. It models the sensing system as a graph and infers unobserved sensor signals from observed sensor data, using randomly sampled subgraphs for scalable learning. As illustrated in the left part of Fig 1, circles denote observed sensors, stars denote unobserved sensors, and the sensors enclosed by the dashed circle form a subgraph sample.

However, in real-world deployments, observed sensors may suffer from missing values due to equipment failures, communication interruptions, and maintenance [17]. For instance, the California Performance Measurement System (PeMS) reports an average missing rate of about 10% across thousands of sensors, and around 15% in Los Angeles [3]. In Beijing’s intelligent transportation system, some loop sensors experience missingness rates of 20% to 25% [24]. Moreover, a New Zealand highway traffic dataset contains many sensor with over 30% missing data. [16].

This situation highlights limitations of existing work. Recent models generally assume fully observed sensors. In practice, missing data at observed sensors violates this assumption. For the **spatial module**, existing methods employ a variety of GNN variants, including GCN-style propagation [38–40], Spatial Aggregation Networks [36, 46], an MPNN backbone [21], and a GIN backbone [19], all of which update node features by aggregating over their neighbors [43]. When neighbors are missing (crudely imputed), the neighborhood mean is biased toward imputed values and local variance

shrinks. This bias and variance shrinkage undermine neighborhood discrimination, causing spatially distinct nodes to become indistinguishable during message aggregation. For the **temporal module**, most models adopt generic sequence modules such as GRU- or RNN-based encoders [10, 25, 45], temporal convolutions [9], or linear temporal filters [21], all of which learn temporal dependencies from continuous input sequences. When long or frequent intervals are missing (crudely imputed), the temporal sequence is dominated by artificial flat segments and abrupt transitions. Such distorted sequences obscure genuine temporal dynamics and hinder the learning of reliable temporal dependencies. To address the aforementioned issues introduced by the missingness at observed sensors, the following key challenges need to be overcome.

C1: Identifiability Issues under Value Source Ambiguity. The same value may originate either from the sensor’s genuine reading or be entirely produced by imputation; Models cannot reliably distinguish the source, resulting in systematic bias in the learned dependency structure for the kriging task. **C2: Heterogeneous and Nonstationary Missingness Regimes.** In real deployments, missingness stems from multiple mechanisms (e.g., random dropouts, maintenance windows, and regional failures). These regimes vary across sensors and over time, which yields structured and nonstationary input corruption. Spatio-temporal dependencies learned under one regime may not generalize to others, so robust learning becomes difficult. **C3: Geometric Distortion under Observation Missingness.** Under observation missingness with crude imputations induces systematic geometric distortion. As formally shown in appendix D.1, missingness followed by fixed-value imputation contracts pairwise distances and collapses the local volume of the data manifold. So the neighborhood-based aggregation and sequence-based temporal modeling are both driven by a surrogate process with reduced variability and distorted transitions. Consequently, the learned spatio-temporal dependencies become weakly identifiable and easily biased.

To address the challenges C1–C3, we propose a robust inductive spatio-temporal kriging framework tailored to scenarios where observed sensors contain missing values. The framework adopts a dual-branch architecture: original observations and their jigsaw-generated virtual-node augmentations are fed into a shared spatio-temporal backbone with explicit missing-mask modulation. More specifically, to address C3, first, we introduce a virtual-node jigsaw augmentation mechanism. We perform controlled replacement only at the positions where observed sensors exhibit missing values. These replacements rely on a dual retrieval process over temporal windows and node similarities. The retrieved donors provide proxy signals that remain consistent with the current spatio-temporal context. Second, we introduce an explicit missing-mask modulation module that treats missingness itself as a key signal governing imputation reliability. This enables the model to distinguish true observations from missing/imputed values, alleviating value source ambiguity (C1). Moreover, it derives reliability- and state-related information from missingness patterns and uses them to condition the model, so the model can adapt its imputation to different missingness regimes (C2). Finally, we introduce an attention-based fusion to dynamically integrate the original and augmented branches, allowing the model to adaptively select the more reliable pathway.

In words, our contributions can be summarized as follows:

- We develop a plug-and-play enhancement framework that can wrap existing inductive spatio-temporal kriging backbones, and achieve consistent improvements across diverse missing patterns on multiple real-world datasets.
- We design a virtual-node jigsaw mechanism that retrieves spatio-temporally similar donor windows and nodes, and synthesizes context-consistent proxy signals only at missing positions.
- We introduce an explicit missingness mask modeling module that encodes missingness patterns as reliability-aware conditioning signals, which enables adaptive inference under heterogeneous missingness.
- We propose a dual-channel attention fusion module to integrate the original and augmented branches, and to adaptively select the more reliable pathway for imputation.

2 Related Works

Spatio-temporal data imputation aims to recover missing values in spatio-temporal sequences and has been widely applied in domains such as traffic and environmental monitoring [42]. Early approaches rely on statistical models such as mean imputation, spline interpolation [22], and regression [26], which struggle to capture complex spatio-temporal dependencies. Recently, GNNs have emerged as a promising paradigm for modeling non-Euclidean spatial structures and temporal dynamics, becoming an important direction for spatio-temporal imputation [37, 44]. From a task perspective, GNN-based imputation can be categorized into in-sample methods and out-of-sample methods, known as spatio-temporal kriging [13, 35].

2.1 In-Sample Imputation

In-sample imputation aims to fill missing values within the observed time series range. GACN [41] integrates the Graph Attention Network (GAT) [31] with temporal convolutions. GRIN [5] employs a spatiotemporal encoder based on Message Passing Neural Networks (MPNN) [8] and Gated Recurrent Units (GRU) [4], using a two-stage process. Bidirectional models such as DGCRIN [15], GARNN [29], and MDGCN [20] differ in their intermediate workflows. The low-rank induced Transformer model ImputeFormer [23] combines low-rank priors with deep learning for heterogeneous data. STAMImputer [33] adopts a Mixture-of-Experts (MoE) framework and low-rank guided graph attention, dynamically generating spatial graphs.

2.2 Out-of-Sample Imputation

Out-of-sample imputation, also known as spatio-temporal kriging, aims to infer missing values at unobserved locations using observed data. In early work, graph-regularized tensor/matrix completion methods have been widely studied for applications [2, 6]. Recent work has shifted toward inductive spatio-temporal kriging (ISK) based on graph neural networks. Early ISK models such as Kriging Convolutional Networks (KCN) [1] and IGNNK [35] demonstrate that treating kriging as a graph signal reconstruction problem enables inductive generalization across graphs and regions. INCREASE [45] introduces multi-relational graphs to capture diverse spatial interactions; KITS [38] and its physics-guided variant

PGITS [40] tackle the graph gap by increment training and physical priors for virtual nodes.

3 Problem Definition

3.1 Spatio temporal Kriging

Let $\mathcal{G} = (\mathcal{V}, \mathcal{E})$ denote a sensor graph with node set \mathcal{V} and edge set \mathcal{E} . We partition the nodes as $\mathcal{V} = \mathcal{V}_o \cup \mathcal{V}_u$, where $|\mathcal{V}_o| = N$ and $|\mathcal{V}_u| = U$ denote the observed and unobserved locations, respectively. For a single feature channel, the measurements at observed locations over T historical time horizon are denoted by $\mathcal{X} \in \mathbb{R}^{N \times T}$, and the ground-truth signals at unobserved locations are denoted by $\mathcal{Y} \in \mathbb{R}^{U \times T}$. The spatial structure of the whole graph is encoded by a weighted adjacency matrix $\mathcal{A} \in [0, 1]^{(N+U) \times (N+U)}$, constructed via a thresholded Gaussian kernel of geographic distances [30]. The goal of spatio-temporal kriging is to estimate \mathcal{Y} from $(\mathcal{X}, \mathcal{A})$.

3.2 Inductive Spatio temporal Kriging

Each subgraph sample contains n observed nodes and u unobserved nodes, where are selected from \mathcal{V}_o and \mathcal{V}_u , with $n \leq N$ and $u \leq U$. For a temporal window of length t , a subgraph sample is represented by (X, A) , where $X \in \mathbb{R}^{(n+u) \times t}$ denotes the input signals on these nodes within the window, and $A \in [0, 1]^{(n+u) \times (n+u)}$ is the adjacency matrix of the induced subgraph. Let \mathcal{F} denote the kriging model, which produces imputations $\hat{Y} = \mathcal{F}(X, A) \in \mathbb{R}^{u \times t}$.

4 Method

4.1 Overview

Given partially observed spatio-temporal signals on a sensor network, our framework wraps an arbitrary inductive spatio-temporal kriging backbone into a unified pipeline, as illustrated in Figure 2. From the raw datasets, we first perform subgraph sampling to obtain the input signals, the weighted adjacency matrix, and the missingness masks. Next, a jigsaw mechanism takes global time series and metadata as inputs, encodes temporal windows and nodes, retrieves similar donors, and constructs a jigsaw-augmented input that replaces only the missing entries while keeping the subgraph structure unchanged. The original and jigsaw-augmented inputs are then fed into a shared backbone to produce dual-channel representations. A missingness-mask module encodes the masks into affine feature transformations and uses them to modulate the features in both channels. Finally, an attention fusion module aggregates the modulated features and outputs the final imputations for unobserved sensors. The entire framework is trained end-to-end with a reconstruction loss and an auxiliary consistency loss that encourages agreement between imputations based on the ground-truth value and the jigsaw-augmented value.

4.2 Virtual-Node Jigsaw Mechanism

In this section, we introduce a jigsaw augmentation mechanism that replaces each missing entry by trajectories retrieved from spatio-temporally similar donor windows. Instead of supplying the backbone with arbitrary imputed values that break the underlying manifold, we always provide proxy signals that lie on real spatio-temporal trajectories, thereby preserving spatial aggregation and temporal trends even in incomplete regions. Proposition D.2 shows

that, under mild conditions on the retrieval quality, the resulting jigsaw estimator enjoys a strictly smaller 2-Wasserstein (optimal transport) distance to the true but unobserved values than crude imputation. Thus, jigsaw augmentation is a principled, distributionally closer reconstruction scheme, which justifies learning a dedicated retrieval module and injecting its virtual-node channel into the kriging pipeline.

4.2.1 Window Encoding Modeling. The virtual node jigsaw augmentation first encodes each temporal window into a compact representation. Over the global horizon, we associate each t steps window with a low-dimensional embedding. Let the time indices be $\{1, \dots, T - t + 1\}$, we form the collection of sliding windows

$$\mathcal{W} = \left\{ \mathcal{I}(\tau) = \{\tau, \dots, \tau + t - 1\} \mid \tau = 1, \dots, T \right\}. \quad (1)$$

For any $\mathcal{I}(\tau) \in \mathcal{W}$, we extract the corresponding observation matrix $X^{(\tau)} \in \mathbb{R}^{N \times t}$ and construct a matrix of periodic time features $P^{(\tau)} \in \mathbb{R}^{t \times d_p}$ for all time steps in the window (e.g., time-of-day and day-of-week, details in appendix B.2), where d_p is the feature dimension. We first aggregate the windowed observations over the node dimension to obtain $\rho(X^{(\tau)}) \in \mathbb{R}^t$. Two linear projections are then applied to $\rho(X^{(\tau)})$ and $P^{(\tau)}$, producing the initialized representations $z_x^{(\tau)} \in \mathbb{R}^{d_r}$ and $z_p^{(\tau)} \in \mathbb{R}^{d_r}$, respectively, which are normalized. We then fuse the two views into a representation. We set

$$h_\tau^{(0)} = \sigma(W_f [z_x^{(\tau)}, z_p^{(\tau)}]^\top + b_f), \quad (2)$$

where σ denotes the activation. Based on $h_\tau^{(0)}$, we apply a shallow multi-layer feed-forward network (FFN) to obtain the final representation $h_\tau^{(l)}$. The window embedding is then defined as the normalized representation $e_\tau \in \mathbb{R}^{d_w}$.

4.2.2 Node Encoding Modeling. In addition to temporal windows, the virtual node jigsaw augmentation encodes each observed node into a representation. The resulting node embeddings summarize functional patterns, exogenous attributes.

For each node $i \in \mathcal{V}_o$, let $X_i \in \mathbb{R}^T$ denote its time series. And we associate a preprocessed exogenous feature vector (details in appendix B.2) $g_i \in \mathbb{R}^{d_e}$, including geographic coordinates, road semantics. Two linear projections are applied to X_i and g_i to obtain initialized representations $z_x^{(i)} \in \mathbb{R}^{d_o}$ and $z_g^{(i)} \in \mathbb{R}^{d_o}$, respectively, which are normalized. The two initialized representations are concatenated and transformed to produce a node-level representation

$$h_i^{(0)} = \sigma(W_c [z_x^{(i)}, z_g^{(i)}]^\top + b_c). \quad (3)$$

And a shallow multi-layer FFN is then applied to obtain $h_i^{(l)}$. Finally, node embedding is defined as $e_i \in \mathbb{R}^{d_n}$ after normalization.

4.2.3 Selection of Replaced and Replacement Sets. Given a spatio-temporal subgraph sample (X, A) , we perform a controlled node-level replacement on observed nodes to construct augmented samples, while keeping the subgraph structure unchanged.

Let the node set of the current subgraph be $\mathcal{V}_s = \mathcal{V}_o^s \cup \mathcal{V}_u^s$, where \mathcal{V}_o^s and \mathcal{V}_u^s denote the sets of observed and unobserved nodes in the subgraph, respectively. Node replacement is restricted to the observed node set \mathcal{V}_o^s . We define the set of replaceable nodes as

$$\mathcal{I}_r = \left\{ i \in \mathcal{V}_o^s \mid m_i \neq \mathbf{1}_t \right\}, \quad (4)$$

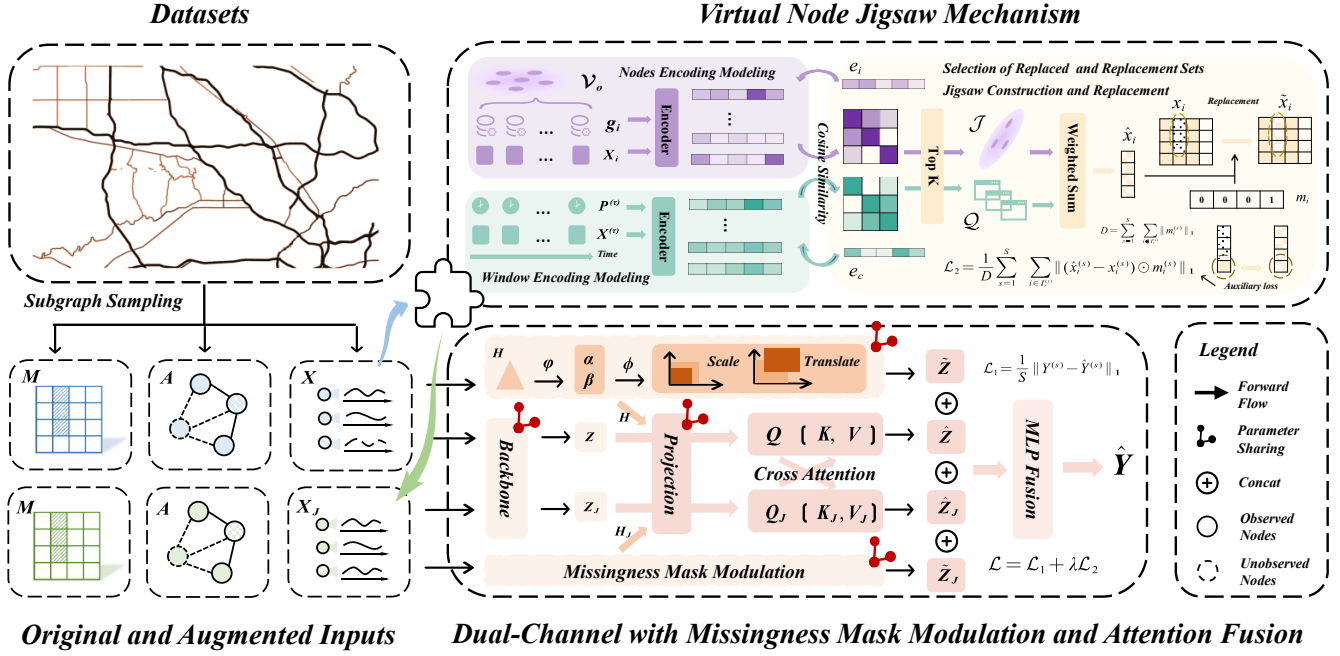


Figure 2: Framework of UniSTOK

where $m_i \in \{0, 1\}^t$ is the temporal observation mask of node i in the current window, and $\mathbf{1}_t$ denotes the all-ones vector of length t . In other words, an observed node is selected for replacement if its current temporal window contains at least one missing entry.

For the current sample, let e_c denote the embedding of its temporal window. Based on the window embeddings, we retrieve a set of similar temporal windows from the global window collection \mathcal{W} , excluding the current window itself:

$$Q = \text{TopK}_{\tau \in \mathcal{W}}(e_c^\top e_\tau), \quad (5)$$

where Q denotes the candidate window set. Meanwhile, for each replaceable node $i \in \mathcal{I}_r$, we retrieve a set of similar donor nodes from the node set \mathcal{V}_o using node embeddings:

$$\mathcal{J}(i) = \text{TopK}_{j \in \mathcal{V}_o}(e_i^\top e_j). \quad (6)$$

4.2.4 Jigsaw Construction and Replacement. Based on the retrieved window set Q and donor node set $\mathcal{J}(i)$, we construct a virtual temporal sequence $\hat{x}_i \in \mathbb{R}^t$ for each $i \in \mathcal{I}_r$. To prevent missing donor values from contributing, for each node $i \in \mathcal{I}_r$, we define a masked and softmax-normalized joint weight vector $w_{\tau,j|i} \in \mathbb{R}^t$ over all candidate nodes $j \in \mathcal{J}(i)$ and candidate windows $\tau \in Q$:

$$w_{\tau,j|i} = \frac{m_j \exp\left(\frac{e_c^\top e_\tau}{\tau_w}\right) \exp\left(\frac{e_i^\top e_j}{\tau_n}\right)}{\sum_{\tau' \in Q} \sum_{j' \in \mathcal{J}(i)} m_{j'} \exp\left(\frac{e_c^\top e_{\tau'}}{\tau_w}\right) \exp\left(\frac{e_i^\top e_{j'}}{\tau_n}\right)}, \quad (7)$$

which represents the normalized contribution of the donor pair (τ, j) to the value of the virtual sequence for node i . The virtual sequence is then computed as

$$\hat{x}_i = \sum_{\tau \in Q} \sum_{j \in \mathcal{J}(i)} w_{\tau,j|i} x_{\tau,j}. \quad (8)$$

Finally, the augmented sequence \tilde{x}_i is obtained by injecting the virtual sequence only at missing positions:

$$\tilde{x}_i = m_i x_i + (1 - m_i) \hat{x}_i, \quad (9)$$

where $\tilde{x}_i \in \mathbb{R}^t, i \in \mathcal{I}_r$. The resulting augmented sample (X_j, A) shares the same subgraph structure and supervision targets as the original sample, differing only in the input signals.

4.3 Missingness Mask Modulation

While jigsaw recovers plausible signals, it does not by itself resolve the value source ambiguity or exploit the information carried by the missingness pattern. In practice, the same numeric value can be either a trustworthy observation or an unreliable imputation, and different missingness regimes often correlate with the underlying target values. To explicitly condition predictions on this reliability structure, we introduce a missingness mask modulation module that encodes the binary mask into a hidden representation and uses it to generate affine modulation parameters that gate the backbone features. D.3 in appendix provides an information-theoretic justification for this design. The derivation reveals that mask conditioning simultaneously reduces bias and variance. Consequently, explicitly modeling the mask as an explicit input is a principled way. This motivates our mask modulation module, which converts the structured missingness pattern into learnable, specific gating signals.

We first encode the missingness mask $M \in \{0, 1\}^{(n+u) \times t}$ and propagate the observed information to the target nodes:

$$H = \varphi(M, X, A), \quad (10)$$

Where φ is an encoder induced by A , yielding hidden representation $H \in \mathbb{R}^{u \times dm}$. Then we generate affine learnable parameters

$$\alpha = \mathbf{1} + \gamma(\phi_\alpha(H)), \quad \beta = \gamma(\phi_\beta(H)), \quad (11)$$

where $\alpha, \beta \in \mathbb{R}^{u \times t}$, ϕ are nonlinear maps and $\gamma > 0$ controls the modulation scale. The additive identity term in α anchors the modulation at the identity mapping, so the transformation starts from a near no-op and only learns bounded deviations when necessary. Finally, We apply the affine modulation

$$\tilde{Z} = \alpha \odot Z + \beta, \quad (12)$$

where $\tilde{Z} \in \mathbb{R}^{u \times t}$ and Z is the backbone output.

4.4 Dual-Channel with Attention Fusion

The virtual-node jigsaw augmentation constructs paired inputs for each subgraph sample, forming two complementary channels. To jointly exploit these dual channels, we design a dual-channel attention fusion module that models the dependency between the two channel outputs and produces a single fused imputation.

4.4.1 Dual Channel. For each subgraph sample, we construct the original input X and the virtual-node-augmented input X_J , forming two parallel channels. Both channels are processed by a backbone to extract spatio-temporal representations $\{Z, Z_J\}$. Subsequently, we apply a missingness mask modulation module to obtain the modulated features $\{\tilde{Z}, \tilde{Z}_J\}$. To be noted, all the mentioned modules are parameter-shared across the two channels.

4.4.2 Cross Attention. To fully leverage the complementary information between the original and augmented branches, we employ an interactive cross-attention mechanism. We reuse the hidden representation $\{H, H_J\}$ as the guidance for attention, while the backbone outputs $\{Z, Z_J\}$ serve as the content. The query, key, and value matrices are projected as follows:

$$Q = HW_q, \quad K = HW_k, \quad V = ZW_v, \quad (13)$$

where $W_q, W_k \in \mathbb{R}^{dm \times dm}$ and $W_v \in \mathbb{R}^{t \times t}$ are learnable parameters. The core of this module is the bidirectional interaction between the two branches. Specifically, the updated representation \hat{Z} for the original branch is generated by querying information from the augmented branch, and vice versa:

$$\hat{Z} = \text{Attn}(Q_J, K, V), \quad \hat{Z}_J = \text{Attn}(Q, K_J, V_J). \quad (14)$$

This cross-attention design allows each branch to calibrate its representation based on the most relevant spatiotemporal patterns captured by its counterpart. In this way, it fuses the raw observations with the virtual-node-augmented observations.

4.4.3 MLP Fusion. After obtaining the interactively calibrated features from the cross-attention module, the fused representation is then passed through a Multi-Layer Perceptron (MLP) to produce the final imputation \hat{Y} :

$$\hat{Y} = \text{MLP}([\hat{Z} \parallel \tilde{Z} \parallel \hat{Z}_J \parallel \tilde{Z}_J]), \quad (15)$$

where $[\cdot \parallel \cdot]$ denotes the concatenation and $\hat{Y} \in \mathbb{R}^{u \times t}$.

4.5 Training Objective with Auxiliary Loss

For each subgraph sample s , we define the primary imputation loss as the Mean Absolute Error (MAE) [34]:

$$\mathcal{L}_1 = \frac{1}{S} \sum_{s=1}^S \|Y^{(s)} - \hat{Y}^{(s)}\|_1, \quad (16)$$

where $\|\cdot\|_1$ sums absolute values over all entries. During virtual-node jigsaw augmentation, each replaceable observed node $i \in I_r^{(s)}$ is associated with a virtual sequence $\hat{x}_i^{(s)}$. To anchor this virtual channel to reliable observations, we impose a masked reconstruction loss that only penalizes discrepancies at available positions. We first count the total number of available entries

$$D = \sum_{s=1}^S \sum_{i \in I_r^{(s)}} \|m_i^{(s)}\|_1, \quad (17)$$

and define the auxiliary loss as

$$\mathcal{L}_2 = \frac{1}{D} \sum_{s=1}^S \sum_{i \in I_r^{(s)}} \|(\hat{x}_i^{(s)} - x_i^{(s)}) \odot m_i^{(s)}\|_1. \quad (18)$$

The final training objective combines the task loss and the masked auxiliary loss:

$$\mathcal{L} = \mathcal{L}_1 + \lambda \mathcal{L}_2, \quad (19)$$

where $\lambda \geq 0$ controls the strength of the auxiliary regularization on the virtual-node channel.

5 Experiments

This section evaluates UniSTOK under heterogeneous missing observations on observed sensors. We answer five research questions:

- **RQ1:** Does integrating strong baselines into our framework consistently improve performance across datasets and missingness patterns?
- **RQ2:** How does our framework compare to a two-stage pipeline (impute observed sensors first, then infer unobserved sensors with baselines)?
- **RQ3:** What is the contribution of each proposed module (via ablation)?
- **RQ4:** How sensitive is performance to key hyperparameters?
- **RQ5:** How robust is the framework under sparse observations and high missing rates?

5.1 Experimental Setup

Datasets. We conduct experiments on three real-world datasets: **METR-LA** and **PEMS-BAY** for traffic speed forecasting, and **NREL-AL** for solar power generation. All datasets are sampled every 5 minutes.

Backbones. We evaluate UniSTOK as a plug-and-play wrapper over five inductive spatio-temporal kriging (ISK) backbones: IGNNK [35], SATCN [36], INCREASE [45], STAGANN [19], and KITS [38]. For each backbone, we report its original performance and the performance after being enhanced by our framework.

Metrics. We report Mean Absolute Error (MAE), Root Mean Squared Error (RMSE), and Mean Absolute Percentage Error (MAPE). MAPE is not reported on NREL because the ground truth contains many zeros, making MAPE unstable and uninformative.

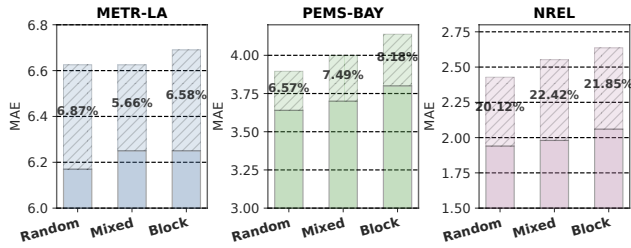


Figure 3: Performance under random, mixed, and block missingness, and the relative gains brought by Ours.

Inductive kriging protocol and missingness simulation. Following the inductive kriging setting, we treat 20% of nodes as *unobserved* nodes (held out from both training and testing inputs). On the remaining *observed* nodes, we inject missing values at a rate of 0.2 under three patterns: **Random**: missing entries are sampled uniformly at random over node-time pairs; **Block**: contiguous time intervals are removed on spatially correlated nodes; **Mixed**: half the missing entries are random, and half are blocked. We use a historical window length $h = 24$ for METR-LA, PEMS-BAY, and NREL. For subgraph sampling, each subgraph contains B observed nodes and one unobserved node (i.e., $U = 1$). The total number of nodes per subgraph are set to 110 (METR-LA), 200 (PEMS-BAY), and 90 (NREL). Other details follow the backbone defaults; full configurations are provided in the appendix B.

5.2 Performance Comparison (RQ1)

To answer **RQ1**, we wrap each ISK backbone with UniSTOK and evaluate them across all datasets and missingness patterns. Table 1 reports absolute errors, comparing each backbone with its UniSTOK-enhanced counterpart. Across all backbones, datasets, and missingness patterns, our framework consistently reduces MAE/RMSE (and MAPE when applicable). This result shows that UniSTOK is backbone-agnostic and improves inductive kriging under missing observations on observed sensors.

Fig. 3 shows a clear dependency on the missingness pattern. Random missingness is the easiest because observations remain temporally scattered, preserving local continuity. Block missingness is the hardest because it removes contiguous intervals and weakens local neighborhood evidence, which directly disrupts both spatial aggregation and temporal modeling.

Fig. 4 summarizes relative improvements across backbones and datasets. The largest gains appear on NREL, where the target series contains many near-zero values and naive imputations can introduce flat artifacts; UniSTOK mitigates this via jigsaw-based proxy signals and mask-aware modulation. Across backbones, INCREASE benefits the most, while stronger backbones such as KITS and STAGANN show smaller but consistent gains. Notably, UniSTOK enables simpler backbones (e.g., INCREASE and SATCN) to reach or surpass the best-performing vanilla baselines, improving the accuracy-efficiency trade-off.

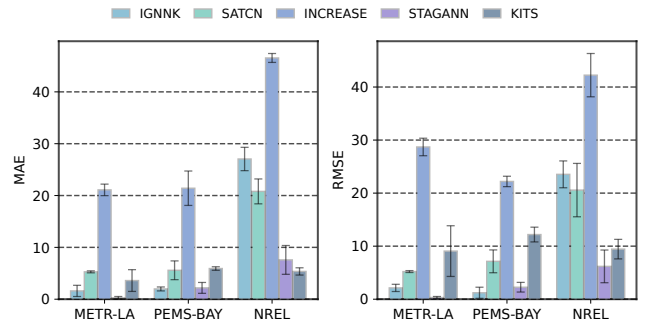


Figure 4: Relative error reduction (%) brought by UniSTOK when applied to different ISK backbones on METR-LA, PEMS-BAY, and NREL.

5.3 Comparison with Pre-Imputation (RQ2)

To answer **RQ2**, we compare UniSTOK with a two-stage pipeline that first imputes missing values on observed sensors and then performs kriging on unobserved sensors. Specifically, we use ImputeFormer [23] to impute observed sensors, followed by STAGANN as the downstream ISK model for unobserved sensors. We evaluate under the **mixed** missing pattern, which combines point-wise corruption and contiguous missing blocks. Table 2 shows that UniSTOK achieves lower MAE and RMSE (and lower MAPE when applicable) on all datasets. This result indicates that end-to-end joint modeling of (i) spatio-temporal dependencies and (ii) missingness-aware reliability is more effective than decoupling imputation and kriging into separate stages.

Table 2: Comparison with a two-stage pre-imputation pipeline under the mixed missing pattern. Bold numbers indicate better performance (lower is better).

Model	Metric	METR-LA	PEMS-BAY	NREL
ImputeFormer+STAGANN	MAE	6.04±0.15	3.84±0.05	1.31±0.05
	RMSE	9.34±0.23	6.76±0.09	2.95±0.19
	MAPE (%)	18.11±0.88	9.14±0.05	-
Ours (UniSTOK)	MAE	5.84±0.05	3.37±0.00	1.16±0.01
	RMSE	9.22±0.05	6.09±0.03	2.41±0.03
	MAPE (%)	16.86±0.13	8.32±0.04	-

5.4 Ablation Study (RQ3)

To answer **RQ3**, we perform ablation studies on METR-LA, PEMS-BAY, and NREL under the mixed missing pattern, using INCREASE as the inductive kriging backbone. We evaluate five variants.

To answer **RQ3**, we perform ablation on METR-LA, PEMS-BAY, and NREL under the mixed missing pattern, using INCREASE (achieves the largest gains in our comparison, which makes the effect of each component more visible) as the backbone. We evaluate five variants: (1) **w/o J+M**: backbone only; (2) **w/o J**: remove jigsaw augmentation; (3) **w/o M**: remove missingness mask modulation; (4) **w/o A**: remove attention fusion; (5) **w/o L**: remove the auxiliary consistency loss. All other settings are kept identical.

As shown in Fig. 5, each component improves performance. Compared with backbone-only (w/o J+M), the full model reduces MAE

Table 1: Performance comparison with different backbones. The green denotes the performance gain brought by our plug-in over the corresponding backbone. MAPE is not reported on the NREL dataset because the ground-truth values contain a large proportion of zeros, which makes it unstable and not informative.

Backbone	Metric	METR-LA			PEMS-BAY			NREL		
		Random	Block	Mixed	Random	Block	Mixed	Random	Block	Mixed
IGNNK + Ours	MAE	6.01±0.01 5.85±0.01 ↓2.7%	6.09±0.01 5.99±0.02 ↓1.6%	6.04±0.02 6.01±0.05 ↓0.5%	3.63±0.02 3.56±0.03 ↓1.9%	3.78±0.00 3.69±0.01 ↓2.4%	3.70±0.02 3.64±0.00 ↓1.6%	2.44±0.02 1.82±0.01 ↓25.4%	2.60±0.03 1.83±0.02 ↓29.6%	2.45±0.00 1.81±0.01 ↓26.1%
	RMSE	9.40±0.01 9.22±0.01 ↓1.9%	9.70±0.01 9.42±0.08 ↓2.9%	9.50±0.01 9.35±0.08 ↓1.6%	6.22±0.03 6.20±0.01 ↓0.3%	6.75±0.01 6.59±0.02 ↓2.4%	6.47±0.00 6.41±0.01 ↓0.9%	4.55±0.03 3.56±0.02 ↓21.8%	4.88±0.02 3.59±0.02 ↓26.4%	4.55±0.02 3.53±0.05 ↓22.4%
	MAPE (%)	17.61±0.08 16.64±0.14 ↓5.5%	18.33±0.04 17.57±0.21 ↓4.1%	17.68±0.03 17.19±0.34 ↓2.8%	8.27±0.06 8.13±0.08 ↓1.7%	9.06±0.01 8.84±0.05 ↓2.4%	8.65±0.00 8.53±0.02 ↓1.4%	-	-	-
SATCN + Ours	MAE	6.11±0.04 5.80±0.04 ↓5.1%	6.26±0.01 5.92±0.06 ↓5.4%	6.17±0.01 5.84±0.05 ↓5.3%	3.55±0.00 3.39±0.00 ↓4.5%	3.73±0.01 3.56±0.00 ↓4.6%	3.65±0.01 3.37±0.00 ↓7.7%	1.76±0.01 1.43±0.00 ↓18.8%	1.88±0.04 1.50±0.00 ↓20.2%	1.92±0.00 1.47±0.02 ↓23.4%
	RMSE	9.65±0.08 9.15±0.10 ↓5.2%	9.98±0.12 9.44±0.00 ↓5.4%	9.71±0.09 9.22±0.05 ↓5.0%	6.37±0.01 6.07±0.01 ↓4.7%	6.93±0.02 6.32±0.10 ↓8.8%	6.69±0.09 6.16±0.01 ↓7.9%	3.41±0.01 2.90±0.01 ↓15.0%	3.90±0.07 3.04±0.03 ↓22.1%	3.97±0.00 2.99±0.02 ↓24.7%
	MAPE (%)	18.21±0.33 16.41±0.10 ↓9.9%	19.00±0.18 17.51±0.11 ↓7.8%	18.23±0.21 17.03±0.16 ↓6.6%	8.37±0.04 8.14±0.02 ↓2.7%	9.27±0.04 8.58±0.19 ↓7.4%	8.87±0.15 8.33±0.01 ↓6.1%	-	-	-
INCREASE + Ours	MAE	7.45±0.03 5.79±0.04 ↓22.3%	7.42±0.01 5.93±0.07 ↓20.1%	7.46±0.00 5.90±0.01 ↓20.9%	4.23±0.01 3.42±0.02 ↓19.1%	4.68±0.01 3.50±0.01 ↓25.2%	4.33±0.03 3.47±0.01 ↓19.9%	3.42±0.00 1.84±0.01 ↓46.2%	3.62±0.00 1.90±0.01 ↓47.5%	3.53±0.00 1.91±0.01 ↓45.9%
	RMSE	13.15±0.05 9.14±0.02 ↓30.5%	13.10±0.01 9.53±0.16 ↓27.3%	13.12±0.05 9.40±0.01 ↓28.3%	7.64±0.01 6.03±0.01 ↓21.1%	8.01±0.03 6.19±0.04 ↓22.7%	7.89±0.01 6.09±0.03 ↓22.8%	5.92±0.02 3.63±0.02 ↓38.7%	6.96±0.04 3.71±0.02 ↓46.7%	6.36±0.00 3.73±0.01 ↓41.4%
	MAPE (%)	26.35±0.09 16.74±0.22 ↓36.5%	26.26±0.01 17.51±0.60 ↓33.3%	26.31±0.06 17.58±0.29 ↓33.2%	11.23±0.25 8.17±0.16 ↓27.2%	12.21±0.21 8.39±0.10 ↓31.3%	11.77±0.39 8.34±0.12 ↓29.1%	-	-	-
STAGANN + Ours	MAE	6.02±0.01 6.02±0.02 ↓0.0%	6.14±0.01 6.11±0.01 ↓0.5%	6.08±0.01 6.06±0.04 ↓0.3%	3.55±0.01 3.51±0.02 ↓1.1%	3.72±0.02 3.60±0.00 ↓3.2%	3.64±0.02 3.56±0.01 ↓2.2%	1.23±0.00 1.16±0.01 ↓5.7%	1.59±0.01 1.49±0.02 ↓6.3%	1.30±0.02 1.16±0.01 ↓10.8%
	RMSE	9.39±0.13 9.35±0.00 ↓0.4%	9.66±0.03 9.65±0.01 ↓0.1%	9.46±0.01 9.42±0.02 ↓0.4%	6.23±0.05 6.15±0.00 ↓1.3%	6.69±0.03 6.53±0.02 ↓2.4%	6.46±0.02 6.26±0.02 ↓3.1%	3.14±0.01 2.43±0.02 ↓4.7%	3.14±0.01 3.01±0.00 ↓4.1%	2.67±0.06 2.41±0.03 ↓9.7%
	MAPE (%)	17.04±0.26 16.55±0.34 ↓2.9%	17.44±0.04 17.40±0.20 ↓0.2%	16.91±0.23 16.86±0.13 ↓0.3%	8.46±0.06 8.09±0.01 ↓4.4%	8.91±0.01 8.77±0.01 ↓1.6%	8.62±0.02 8.32±0.04 ↓3.5%	-	-	-
KITS + Ours	MAE	6.46±0.17 6.18±0.02 ↓4.3%	6.49±0.01 6.15±0.04 ↓5.2%	6.49±0.04 6.41±0.04 ↓1.2%	3.90±0.00 3.66±0.02 ↓6.2%	3.98±0.01 3.76±0.03 ↓5.5%	3.94±0.00 3.70±0.01 ↓6.1%	2.19±0.01 2.09±0.01 ↓4.6%	2.13±0.05 2.01±0.03 ↓5.6%	2.21±0.09 2.08±0.06 ↓5.9%
	RMSE	11.01±0.23 9.58±0.19 ↓13.0%	11.07±0.01 9.91±0.06 ↓10.5%	10.97±0.02 10.56±0.09 ↓3.7%	7.44±0.09 6.49±0.04 ↓12.8%	7.73±0.04 6.71±0.14 ↓13.2%	7.54±0.13 6.74±0.00 ↓10.6%	4.16±0.03 3.85±0.09 ↓7.5%	4.24±0.07 3.77±0.02 ↓11.1%	4.29±0.15 3.87±0.20 ↓9.8%
	MAPE (%)	22.06±0.64 18.55±0.78 ↓16.0%	22.22±0.06 19.24±0.22 ↓13.4%	22.09±0.15 20.91±0.94 ↓5.3%	10.30±0.05 8.69±0.06 ↓15.6%	10.62±0.06 9.07±0.19 ↓14.6%	10.38±0.15 9.06±0.01 ↓12.7%	-	-	-

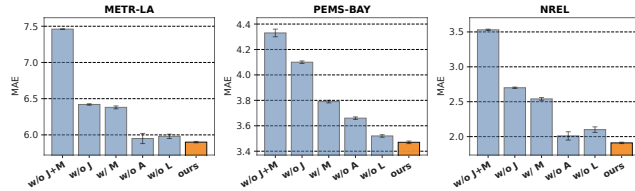


Figure 5: Ablation study (INCREASE backbone, mixed missingness). Removing Jigsaw or Mask modulation causes the largest degradation; Attention fusion and the auxiliary loss provide additional improvements.

by 20.9% (METR-LA), 19.9% (PEMS-BAY), and 45.9% (NREL). Removing jigsaw augmentation (w/o J) or mask modulation (w/o M) leads to the largest error increase, confirming that (i) context-consistent proxy signals and (ii) explicit missingness-aware conditioning are both necessary and complementary. Removing attention fusion (w/o A) and removing the auxiliary loss (w/o L) also increase errors, with w/o L being particularly harmful on NREL, indicating that enforcing cross-channel consistency is important when the data contain many near-zero regimes.

5.5 Hyperparameter Sensitivity Analysis (RQ4)

To answer RQ4, we study hyperparameter sensitivity on METR-LA under the mixed missing pattern using IGNNK as the backbone. We sweep four key hyperparameters: the auxiliary-loss weight λ , the mask-modulation scale γ , and the retrieval sizes (top- k donor nodes and top- k donor windows) in the jigsaw module. We vary one hyperparameter at a time while keeping the others fixed.

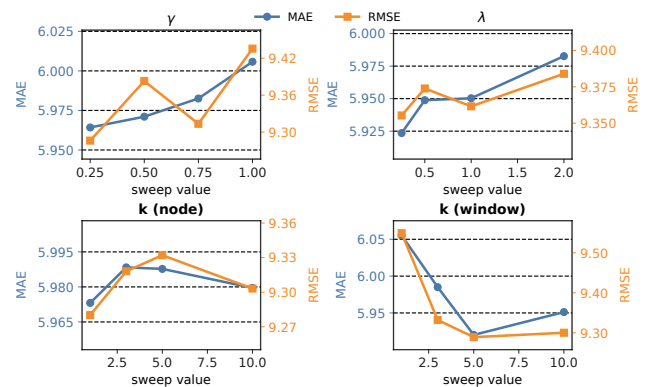


Figure 6: Hyperparameter sensitivity on METR-LA (mixed missingness, IGNNK backbone). MAE/RMSE change mildly across a wide range of λ , γ , and retrieval sizes, indicating stable performance without delicate tuning.

Fig. 6 shows that UniSTOK is not sensitive to hyperparameter choices. MAE and RMSE vary only slightly when sweeping λ and γ , indicating that the auxiliary loss and mask modulation are consistently beneficial across a broad range. Performance is also stable across retrieval sizes; moderate top- k values typically perform best, reflecting a practical trade-off between donor relevance and diversity. We observe similar trends for other backbones; results are reported in the appendix C.

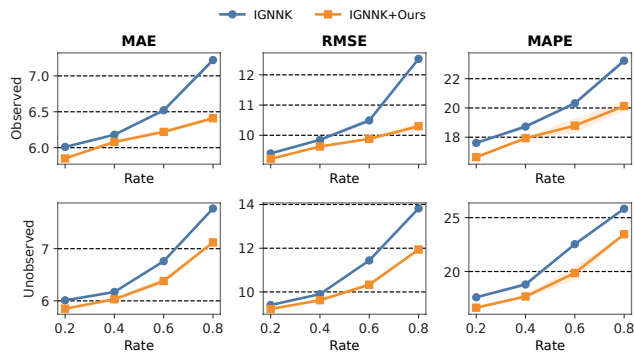


Figure 7: Robustness on METR-LA (IGNNK backbone). UniSTOK consistently outperforms the vanilla backbone as (i) the missing rate on observed sensors increases (first row) and (ii) the unobserved-node ratio increases (second row).

5.6 Robustness under Sparse Observed Sensors and High Missing Rates (RQ5)

To answer RQ5, we evaluate robustness on METR-LA using IGNNK as the backbone under two stress tests. **(1) Sparse observations:** we increase the ratio of unobserved sensors from 0.2 to 0.8, reducing the number of sensors available for inference. **(2) Severe missingness:** we increase the missing rate on observed sensors from 0.2 to 0.8, corrupting inputs more aggressively.

As shown in Fig. 7, both stress tests consistently degrade the vanilla IGNNK across MAE/RMSE/MAPE, confirming that inductive kriging becomes harder with fewer and noisier observations. UniSTOK remains better across all settings and exhibits a slower degradation trend, demonstrating improved robustness to both observation sparsity and missingness severity.

5.7 Case Study: What Does Jigsaw Retrieve?

To interpret the learned retrieval behavior, we analyze (i) which temporal windows are retrieved for a given anchor window and (ii) which donor nodes are retrieved for a given anchor node.

5.7.1 Temporal window retrieval. For each anchor window, we collect its top- K retrieved donor windows and compute their time-of-day offset (the difference in their positions within the daily cycle). We aggregate offsets over all anchor windows and report the distributions in Fig. 8.

All distributions peak sharply at zero, meaning that the retriever preferentially selects donor windows occurring at nearly the same daily phase as the anchor. This behavior is consistent across random, mixed, and block missingness, showing that temporal retrieval is stable under different corruption regimes. Therefore, the jigsaw module learns an interpretable temporal prior: it reconstructs a partially observed window by borrowing trajectories from other days with matched periodic context.

5.7.2 Node retrieval. We visualize the spatial donors on the road network. For a representative sensor (red star in Fig. 9), we plot the top- K donor nodes (blue dots) selected by the node-level retriever along with all sensors (gray).

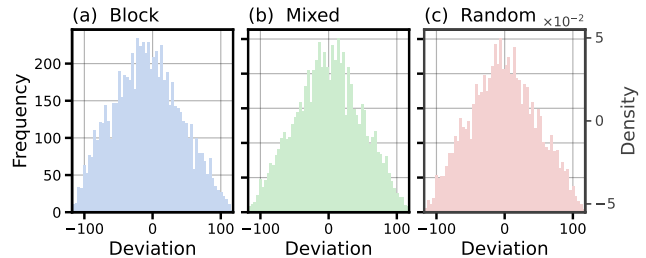


Figure 8: Time-of-day offset between each anchor window and its top- K retrieved donor windows. Offsets concentrate around zero across all missingness patterns, indicating retrieval prefers windows with similar daily phase.



Figure 9: Top- K donor nodes retrieved for an anchor sensor (Sensor 24 marked by red stars). Most donors are geographically local, with occasional farther donors on functionally similar road segments.

Most retrieved donors lie on nearby road segments, indicating that the retriever prioritizes local spatial correlation. The occasional distant donors typically appear on major highways or parallel arterials, suggesting that the retriever also captures functional similarity beyond pure geographic distance.

6 Conclusion

In this work, we addressed the practical but underexplored setting of inductive spatio-temporal kriging (ISK) with partially observed sensors that themselves suffer from missingness. We proposed UniSTOK, a plug-and-play framework that wraps arbitrary ISK backbones with a virtual-node jigsaw augmentation mechanism, a missingness mask modulation module, and a dual-channel attention fusion module, enabling baselines to better exploit heterogeneous missingness patterns and alleviate disrupted spatio-temporal structure. Extensive experiments on multiple real-world datasets, various missing patterns, show that UniSTOK consistently improves imputation accuracy and robustness over both vanilla backbones and strong pre-imputation pipelines, including in challenging cases with sparse observed sensors or high missing rates.

References

- [1] Gabriel Appleby, Linfeng Liu, and Li-Ping Liu. 2020. Kriging convolutional networks. In *Proceedings of the AAAI conference on artificial intelligence*, Vol. 34. 3187–3194.
- [2] Joan Bruna, Wojciech Zaremba, Arthur Szlam, and Yann LeCun. 2013. Spectral networks and locally connected networks on graphs. *arXiv preprint arXiv:1312.6203* (2013).
- [3] Chao Chen, Jaimyoung Kwon, John Rice, Alexander Skabardonis, and Pravin Varaiya. 2003. Detecting errors and imputing missing data for single-loop surveillance systems. *Transportation Research Record* 1855, 1 (2003), 160–167.
- [4] Junyoung Chung, Caglar Gulcehre, KyungHyun Cho, and Yoshua Bengio. 2014. Empirical evaluation of gated recurrent neural networks on sequence modeling. *arXiv preprint arXiv:1412.3555* (2014).
- [5] Andrea Cini, Ivan Marisca, and Cesare Alippi. 2021. Filling the g_{ap_s} : Multivariate time series imputation by graph neural networks. *arXiv preprint arXiv:2108.00298* (2021).
- [6] Dingxiong Deng, Cyrus Shahabi, Ugur Demiryurek, Linhong Zhu, Rose Yu, and Yan Liu. 2016. Latent space model for road networks to predict time-varying traffic. In *Proceedings of the 22nd ACM SIGKDD international conference on knowledge discovery and data mining*, 1525–1534.
- [7] Aya Ferchichi, Ahlem Ferchichi, Fatma Hendaoui, Mejda Chihaoui, and Radhia Toujani. 2025. Deep learning-based uncertainty quantification for spatio-temporal environmental remote sensing: A systematic literature review. *Neurocomputing* (2025), 130242.
- [8] Justin Gilmer, Samuel S Schoenholz, Patrick F Riley, Oriol Vinyals, and George E Dahl. 2017. Neural message passing for quantum chemistry. In *International conference on machine learning*. Pmlr, 1263–1272.
- [9] Junfeng Hu, Yuxuan Liang, Zhencheng Fan, Hongyang Chen, Yu Zheng, and Roger Zimmermann. 2023. Graph neural processes for spatio-temporal extrapolation. In *Proceedings of the 29th ACM SIGKDD Conference on Knowledge Discovery and Data Mining*, 752–763.
- [10] Junfeng Hu, Yuxuan Liang, Zhencheng Fan, Li Liu, Yifang Yin, and Roger Zimmermann. 2023. Decoupling long-and short-term patterns in spatiotemporal inference. *IEEE Transactions on Neural Networks and Learning Systems* (2023).
- [11] Weiwei Jiang and Jiayun Luo. 2022. Graph neural network for traffic forecasting: A survey. *Expert systems with applications* 207 (2022), 117921.
- [12] Guangyin Jin, Yuxuan Liang, Yuchen Fang, Zezhi Shao, Jincai Huang, Junbo Zhang, and Yu Zheng. 2023. Spatio-temporal graph neural networks for predictive learning in urban computing: A survey. *IEEE transactions on knowledge and data engineering* 36, 10 (2023), 5388–5408.
- [13] Ming Jin, Huan Yee Koh, Qingsong Wen, Daniele Zambon, Cesare Alippi, Geoffrey I Webb, Irwin King, and Shirui Pan. 2024. A survey on graph neural networks for time series: Forecasting, classification, imputation, and anomaly detection. *IEEE Transactions on Pattern Analysis and Machine Intelligence* (2024).
- [14] TN Kipf. 2016. Semi-Supervised Classification with Graph Convolutional Networks. *arXiv preprint arXiv:1609.02907* (2016).
- [15] Xiangjie Kong, Wenfeng Zhou, Guojiang Shen, Wenyi Zhang, Nali Liu, and Yao Yang. 2023. Dynamic graph convolutional recurrent imputation network for spatiotemporal traffic missing data. *Knowledge-Based Systems* 261 (2023), 110188.
- [16] Bo Li, Ruotao Yu, Zijun Chen, Yingzhe Ding, Mingxia Yang, Jinghua Li, Jianxiao Wang, and Haiwang Zhong. 2024. High-resolution multi-source traffic data in New Zealand. *Scientific Data* 11, 1 (2024), 1216.
- [17] Huiping Li, Meng Li, Xi Lin, Fang He, and Yinhai Wang. 2020. A spatiotemporal approach for traffic data imputation with complicated missing patterns. *Transportation research part C: emerging technologies* 119 (2020), 102730.
- [18] Yaguang Li, Rose Yu, Cyrus Shahabi, and Yan Liu. 2017. Diffusion convolutional recurrent neural network: Data-driven traffic forecasting. *arXiv preprint arXiv:1707.01926* (2017).
- [19] Yujie Li, Shao Zezhi, Chengqing Yu, Tangwen Qian, Zhao Zhang, Yifan Du, Shaoming He, Fei Wang, and Yongjun Xu. 2025. Sta-gann: A valid and generalizable spatio-temporal kriging approach. In *Proceedings of the 34th ACM International Conference on Information and Knowledge Management*, 1726–1736.
- [20] Yuebing Liang, Zhan Zhao, and Lijun Sun. 2022. Memory-augmented dynamic graph convolution networks for traffic data imputation with diverse missing patterns. *Transportation Research Part C: Emerging Technologies* 143 (2022), 103826.
- [21] Zhuoxuan Liang, Wei Li, Dalin Zhang, Yidan Chen, Zhihong Wang, Xiangping Zheng, and Moustafa Youssef. 2025. DarkFarseeer: Inductive Spatio-temporal Kriging via Hidden Style Enhancement and Sparsity-Noise Mitigation. *arXiv preprint arXiv:2501.02808* (2025).
- [22] Sky McKinley and Megan Levine. 1998. Cubic spline interpolation. *College of the Redwoods* 45, 1 (1998), 1049–1060.
- [23] Tong Nie, Guoyang Qin, Wei Ma, Yuewen Mei, and Jian Sun. 2024. ImputeFormer: Low rankness-induced transformers for generalizable spatiotemporal imputation. In *Proceedings of the 30th ACM SIGKDD conference on knowledge discovery and data mining*, 2260–2271.
- [24] Li Qu, Li Li, Yi Zhang, and Jianming Hu. 2009. PPCA-based missing data imputation for traffic flow volume: A systematical approach. *IEEE Transactions on intelligent transportation systems* 10, 3 (2009), 512–522.
- [25] Andreas Roth and Thomas Liebig. 2022. Forecasting unobserved node states with spatio-temporal graph neural networks. In *2022 IEEE International Conference on Data Mining Workshops (ICDMW)*. IEEE, 740–747.
- [26] Muhammad Saad, Mohita Chaudhary, Fakhri Karray, and Vincent Gaudet. 2020. Machine learning based approaches for imputation in time series data and their impact on forecasting. In *2020 IEEE International Conference on Systems, Man, and Cybernetics (SMC)*. IEEE, 2621–2627.
- [27] Zezhi Shao, Zhao Zhang, Fei Wang, and Yongjun Xu. 2022. Pre-training enhanced spatial-temporal graph neural network for multivariate time series forecasting. In *Proceedings of the 28th ACM SIGKDD conference on knowledge discovery and data mining*, 1567–1577.
- [28] Zezhi Shao, Zhao Zhang, Wei Wei, Fei Wang, Yongjun Xu, Xin Cao, and Christian S Jensen. 2022. Decoupled dynamic spatial-temporal graph neural network for traffic forecasting. *arXiv preprint arXiv:2206.09112* (2022).
- [29] Guojiang Shen, Wenfeng Zhou, Wenyi Zhang, Nali Liu, Zhi Liu, and Xiangjie Kong. 2023. Bidirectional spatial-temporal traffic data imputation via graph attention recurrent neural network. *Neurocomputing* 531 (2023), 151–162.
- [30] David I Shuman, Sunil K Narang, Pascal Frossard, Antonio Ortega, and Pierre Vandergheynst. 2013. The emerging field of signal processing on graphs: Extending high-dimensional data analysis to networks and other irregular domains. *IEEE signal processing magazine* 30, 3 (2013), 83–98.
- [31] Petar Veličković, Guillem Cucurull, Arantxa Casanova, Adriana Romero, Pietro Lio, and Yoshua Bengio. 2017. Graph attention networks. *arXiv preprint arXiv:1710.10903* (2017).
- [32] Pengkun Wang, Chaochao Zhu, Xu Wang, Zhengyang Zhou, Guang Wang, and Yang Wang. 2022. Inferring intersection traffic patterns with sparse video surveillance information: An st-gan method. *IEEE Transactions on Vehicular Technology* 71, 9 (2022), 9840–9852.
- [33] Yiming Wang, Hao Peng, Senzhang Wang, Haohua Du, Chunyang Liu, Jia Wu, and Guanlin Wu. 2025. STAMImputer: Spatio-Temporal Attention MoE for Traffic Data Imputation. *arXiv preprint arXiv:2506.08054* (2025).
- [34] Cort J Willmott and Kenji Matsuura. 2005. Advantages of the mean absolute error (MAE) over the root mean square error (RMSE) in assessing average model performance. *Climate research* 30, 1 (2005), 79–82.
- [35] Yuankai Wu, Dingyi Zhuang, Aurelie Labbe, and Lijun Sun. 2021. Inductive graph neural networks for spatiotemporal kriging. In *Proceedings of the AAAI conference on artificial intelligence*, Vol. 35. 4478–4485.
- [36] Yuankai Wu, Dingyi Zhuang, Mengying Lei, Aurelie Labbe, and Lijun Sun. 2021. Spatial aggregation and temporal convolution networks for real-time kriging. *arXiv preprint arXiv:2109.12144* (2021).
- [37] Zonghan Wu, Shirui Pan, Fengwen Chen, Guodong Long, Chengqi Zhang, and Philip S Yu. 2020. A comprehensive survey on graph neural networks. *IEEE transactions on neural networks and learning systems* 32, 1 (2020), 4–24.
- [38] Qianxiang Xu, Cheng Long, Ziyue Li, Sijie Ruan, Rui Zhao, and Zhishuai Li. 2025. Kits: Inductive spatio-temporal kriging with increment training strategy. In *Proceedings of the AAAI Conference on Artificial Intelligence*, Vol. 39. 12945–12953.
- [39] Chen Yang, Changhao Zhao, Chen Wang, and Jiansheng Fan. 2025. DRiK: Distribution-Robust Inductive Kriging without Information Leakage. *arXiv preprint arXiv:2509.23631* (2025).
- [40] Songlin Yang, Tao Yang, and Bo Hu. 2025. Inductive Spatio-Temporal Kriging with Physics-Guided Increment Training Strategy for Air Quality Inference. *arXiv preprint arXiv:2503.09646* (2025).
- [41] Yongchao Ye, Shiyao Zhang, and James JQ Yu. 2021. Spatial-temporal traffic data imputation via graph attention convolutional network. In *International Conference on artificial neural networks*. Springer, 241–252.
- [42] Ye Yuan, Yong Zhang, Boyue Wang, Yuan Peng, Yongli Hu, and Baocai Yin. 2022. STGAN: Spatio-temporal generative adversarial network for traffic data imputation. *IEEE Transactions on Big Data* 9, 1 (2022), 200–211.
- [43] Haoyu Zhang, Daoli Wang, Wangshu Zhao, Zitong Lu, and Xuchu Jiang. 2025. IMCSN: An improved neighborhood aggregation interaction strategy for multi-scale contrastive Siamese networks. *Pattern Recognition* 158 (2025), 111052.
- [44] Haoyu Zhang, Wentao Zhang, Hao Miao, Xinke Jiang, Yuchen Fang, and Yifan Zhang. 2025. STRAP: Spatio-Temporal Pattern Retrieval for Out-of-Distribution Generalization. *arXiv:2505.19547 [cs.LG]* <https://arxiv.org/abs/2505.19547>
- [45] Chuanpan Zheng, Xiaoliang Fan, Cheng Wang, Jianzhong Qi, Chaochao Chen, and Longbiao Chen. 2023. Increase: Inductive graph representation learning for spatio-temporal kriging. In *Proceedings of the ACM Web Conference 2023*, 673–683.
- [46] Qishen Zhou, Yifan Zhang, Michail A Makridis, Anastasios Kouvelas, Yibing Wang, and Simon Hu. 2025. MoGERNN: An inductive traffic predictor for unobserved locations. *Transportation Research Part C: Emerging Technologies* 174 (2025), 105080.

A Notation

The main notations used in this paper are summarized in Table 3.

B Implementation Details

B.1 Adjacency matrix

For the distance-based adjacency matrix, we build the adjacency matrix following [18] as follows:

$$A_{ij} = \exp\left(-\left(\frac{\text{dist}(v_i, v_j)}{\sigma}\right)^2\right) \quad (20)$$

where A_{ij} represents the weight between sensors v_i and v_j in the adjacency matrix, $\text{dist}(v_i, v_j)$ denotes the geographical distance between the two sensors, and σ is a scaling factor that adjusts how distances are translated into weights. This method ensures that closer sensors have higher connection weights, reflecting their stronger potential interaction or similarity.

B.2 Metadata

For temporal metadata, all three datasets are sampled every 5 minutes, so a day comprises 288 equidistant indices. We parameterize time by its phase on the daily circle. Let t denote the time-of-day in minutes since midnight, $t \in \{0, 5, \dots, 24 \times 60 - 5\}$, and define the normalized phase $p_t = t/(24 \times 60) \in [0, 1)$. The temporal descriptor is given by the trigonometric embedding

$$\phi_{\text{time}}(t) = (p_t, \sin(2\pi p_t), \cos(2\pi p_t)) \in \mathbb{R}^{d_p}, \quad (21)$$

with $d_p = 3$. The same encoding ϕ_{time} is used for all three datasets.

For node-level metadata, each sensor is associated with its geographical location. Let $c_i = (x_i, y_i) \in \mathbb{R}^2$ denote the raw coordinate of node i . Within each dataset we apply feature-wise min-max normalization to obtain $\tilde{c}_i \in [0, 1]^2$, which yields a 2-dimensional spatial metadata vector shared by all datasets.

For the METR-LA dataset, we further augment each node with road attributes. For node i , we load a categorical feature vector $a_i \in \{0, 1\}^9$, where the first 7 components form a one-hot encoding of the road type and the last 2 components form a one-hot encoding of the road functional class. The final node metadata is given by

$$m_i = \begin{cases} (\tilde{c}_i, a_i) \in \mathbb{R}^{d_e}, & \text{for METR-LA,} \\ \tilde{c}_i \in \mathbb{R}^{d_e}, & \text{for the other two datasets,} \end{cases} \quad (22)$$

with $d_e = 11$ for METR-LA and $d_e = 2$ otherwise.

B.3 Backbones and Hyperparameters

IGNNK [35] Inductive Graph Neural Network Kriging is one of the earliest inductive ST-kriging models that applies graph neural networks on randomly sampled subgraphs to reconstruct full-node signals, thereby learning a transferable message-passing mechanism for interpolation on unseen nodes and graphs. *Hyperparameters*: We stack three diffusion graph convolution layers. In our implementation, the hidden dimension is set to $z = 64$, and the Chebyshev diffusion order is fixed to $K = 2$ for all datasets.

SATCN [36] Spatial Aggregation and Temporal Convolution Networks combines multi-aggregator spatial graph networks with temporal convolutional modules to capture spatial and temporal dependencies, and adopts masking and inductive training strategies to

enable kriging on unobserved locations without relying on a fixed graph structure. *Hyperparameters*: We use $B = 2$ stacked SATCN blocks, as suggested by the original paper. Each block has $c = 32$ hidden units in both the spatial aggregation network and the temporal convolution network, and the TCN kernel size is set to $k_{\text{tcn}} = 3$.

INCREASE [45] Inductive Graph Representation Learning for Spatio-Temporal Kriging constructs multiple heterogeneous spatial graphs (e.g., spatial proximity, functional similarity, transition probability) and employs relation-aware GRU and multi-relation attention to learn spatio-temporal representations that generalize to new locations. *Hyperparameters*: We adopt the spatial variant with hidden state dimension $D = 64$, consistent with the original setting. For each relation-specific graph, we aggregate information from the top- $k = 8$ neighbors, and use a single-layer relation-aware GRU.

STA-GANN [19] Spatio-Temporal Aware Graph Adversarial Neural Network introduces a phase-decoupling module, dynamic metadata graph modeling, and adversarial transfer learning to better capture dynamic spatial dependencies and temporal shifts, improving robustness and generalization to unseen sensors. *Hyperparameters*: We use an encoder with $L = 3$ layers and temporal convolution kernel size $k_{\text{temp}} = 3$. The dimension of node and dynamic-graph embeddings is set to $d_{\text{emb}} = 32$. The adversarial loss is added with weight $\lambda_{\text{adv}} = 0.1$, and the gradient reversal coefficient is linearly warmed up to $\lambda_{\text{GRL}} = 1.0$ over the first 10 epochs.

KITS [38] Kriging with Increment Training Strategy incrementally adds virtual nodes with pseudo labels during training to narrow the gap between training and inference graphs, thereby enhancing the inductive kriging performance when real unseen nodes appear in the test graph. *Hyperparameters*: In the KITS, the channel dimension of all graph and temporal modules is set to $D = 64$. The temporal stacking window length is fixed to $T = 13$ (an odd number), and we empirically set the weight of the neighborhood consistency regularizer to $\lambda_{\text{NCR}} = 0.1$ during Stage 2 training.

B.4 Parameter learning

All experiments were conducted using the optimizer with an initial learning rate of 0.001, which was decayed by a factor of 0.5 every 20 epochs. The batch size was set to 128. To obtain the optimal model for testing, we used a validation combined with an early stopping strategy with a patience of 20 epochs.

C Additional Experimental Results

As shown in Figs. 10–13, the method is generally robust: MAE/RMSE vary only mildly across a wide range of λ , γ , and retrieval sizes, indicating stable performance without delicate hyperparameter tuning.

Symbol	Description
<i>Global problem setup</i>	
$\mathcal{G} = (\mathcal{V}, \mathcal{E})$	Sensor graph with node set \mathcal{V} and edge set \mathcal{E} .
$\mathcal{V}_o, \mathcal{V}_u$	Sets of observed and unobserved locations, with $\mathcal{V} = \mathcal{V}_o \cup \mathcal{V}_u$.
N, U	Numbers of observed and unobserved locations, $N = \mathcal{V}_o $ and $U = \mathcal{V}_u $.
T	Number of time steps in a temporal window.
$\mathcal{X} \in \mathbb{R}^{N \times T}$	Measurements at observed locations over T time steps (single feature channel).
$\mathcal{Y} \in \mathbb{R}^{U \times T}$	Ground-truth signals at unobserved locations.
$\mathcal{A} \in [0, 1]^{(N+U) \times (N+U)}$	Weighted adjacency matrix encoding spatial structure.
<i>Subgraphs sample</i>	
\mathcal{V}_s	Node set of the s -th sampled spatio-temporal subgraph.
$\mathcal{V}_o^s, \mathcal{V}_u^s$	Observed and unobserved node sets in subgraph s .
n, u	Numbers of observed and unobserved nodes in subgraph s , $n = \mathcal{V}_o^s $, $u = \mathcal{V}_u^s $.
t	Number of historical time horizon.
$X \in \mathbb{R}^{(n+u) \times t}$	Input signals on the nodes of a subgraph over the temporal window.
$X_J \in \mathbb{R}^{(n+u) \times t}$	Jigsaw-augmented input signals on the nodes of a subgraph over the temporal window.
$A \in [0, 1]^{(n+u) \times (n+u)}$	Adjacency matrix of the induced subgraph.
$Y \in \mathbb{R}^{u \times t}$	Ground-truth signals on unobserved nodes in the subgraph.
$\hat{Y} \in \mathbb{R}^{u \times t}$	Model imputation on unobserved nodes in the subgraph.
$x_i \in \mathbb{R}^t$	Original temporal signal of node i in the current subgraph window.
$\hat{x}_i \in \mathbb{R}^t$	Jigsaw-augmented (virtual) temporal sequence of node i .
$m_i \in \{0, 1\}^t$	Within-window availability mask of node i (1 if observed, 0 if missing).
<i>Model-specific</i>	
\mathcal{W}	Collection of sliding temporal windows over the global horizon.
$X^{(\tau)}$	Windowed observation matrix over all observed nodes for window.
$P^{(\tau)}$	Matrix of periodic/time-of-day features for window.
$e_\tau \in \mathbb{R}^{d_w}$	Window embedding for window.
$X_i \in \mathbb{R}^T$	Time series of observed node i over the global horizon.
$g_i \in \mathbb{R}^{d_e}$	Preprocessed exogenous feature vector of node i .
$e_i \in \mathbb{R}^{d_n}$	Node embedding of node i .
\mathcal{Q}	Retrieved candidate window set for the current window
$\mathcal{J}_{(i)}$	Retrieved donor node set for node i .
α, β	Learnable modulation parameter for mask modulation.
γ	Positive scalar controlling the magnitude of mask modulation
Z	Backbone output.
\tilde{Z}	Affine-modulated output.
\hat{Z}	Attention output.
Q, K, V	Query, key, and value matrices in the attention mechanism.

Table 3: Summary of main notation used in this paper.

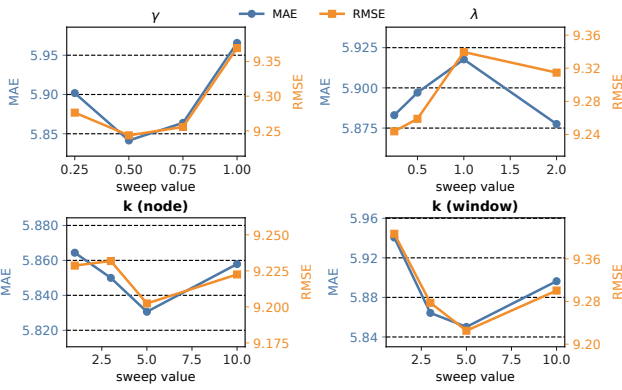


Figure 10: Hyperparameter sensitivity on METR-LA (mixed missingness, SACTN backbone). MAE/RMSE change mildly across a wide range of λ , γ , and retrieval sizes, indicating stable performance without delicate tuning.

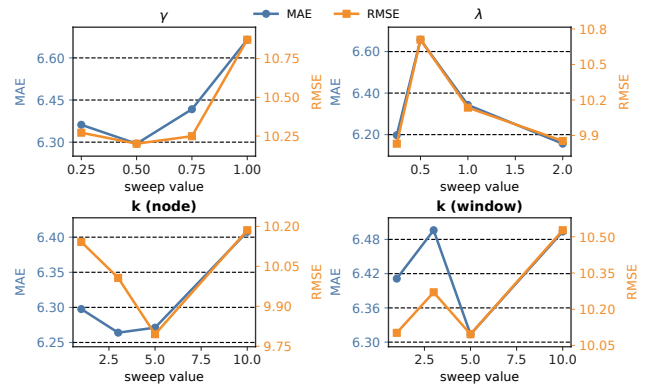


Figure 12: Hyperparameter sensitivity on METR-LA (mixed missingness, KITS backbone). MAE/RMSE change mildly across a wide range of λ , γ , and retrieval sizes, indicating stable performance without delicate tuning.

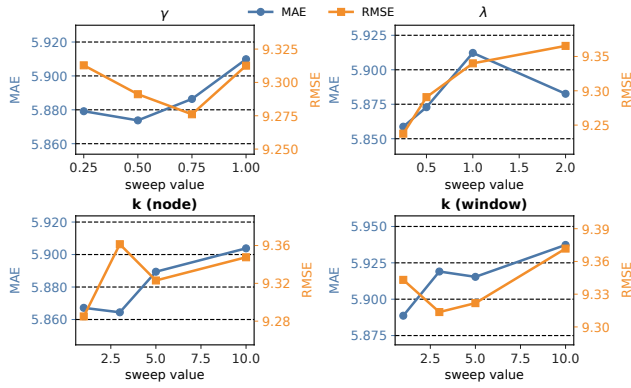


Figure 11: Hyperparameter sensitivity on METR-LA (mixed missingness, INCREASE backbone). MAE/RMSE change mildly across a wide range of λ , γ , and retrieval sizes, indicating stable performance without delicate tuning.

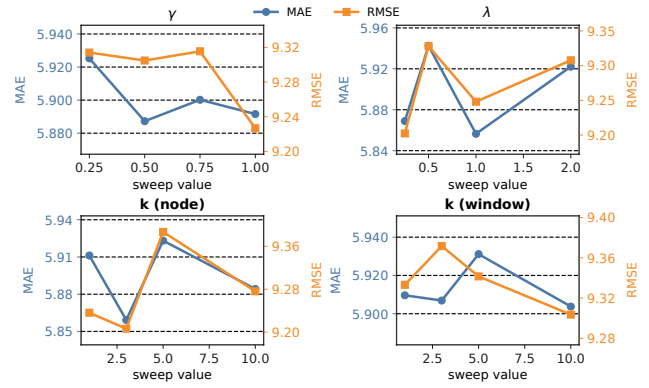


Figure 13: Hyperparameter sensitivity on METR-LA (mixed missingness, STAGANN backbone). MAE/RMSE change mildly across a wide range of λ , γ , and retrieval sizes, indicating stable performance without delicate tuning.

D Proposition and Proof

PROPOSITION D.1 (GEOMETRIC DISTORTION UNDER MISSING DATA). Let $\mathcal{M} \subset \mathbb{R}^n$ be the manifold of sensor observations equipped with the Euclidean metric. Under random missingness with rate $p \in (0, 1)$ and deterministic imputation $z \in \mathbb{R}^n$, the observed manifold $\tilde{\mathcal{M}}$ satisfies:

(1) **Distance Contraction.** For any $x, y \in \mathcal{M}$,

$$\mathbb{E}[\|\tilde{x} - \tilde{y}\|^2] = (1-p)\|x - y\|^2 + p\|z_x - z_y\|^2, \quad (23)$$

where $\tilde{x} = \Pi_p x + (I - \Pi_p)z_x$ and $\Pi_p = \text{diag}(r_1, \dots, r_n)$ with $r_i \sim \text{Bernoulli}(1-p)$ i.i.d.

(2) **Volume Collapse.** The expected volume element satisfies

$$\mathbb{E}[d\tilde{V}] = (1-p)^{n/2}dV + O(p\sqrt{n}), \quad (24)$$

where dV is the volume element on \mathcal{M} .

PROOF. We prove both statements by direct calculation of expectations over the random missingness process. The key idea is to decompose the imputed observations into observed and imputed components, then use the independence of missingness indicators to compute moments. For Part 1, we expand the squared distance and separate terms by missingness patterns. For Part 2, we use the fact that the volume element is the square root of the metric determinant, which factors under diagonal transformations.

We model the observation process as follows. Let $x = (x_1, \dots, x_n)^T \in \mathbb{R}^n$ be the true observation vector at a sensor node. The missingness pattern is encoded by a random diagonal matrix:

$$\Pi_p = \text{diag}(r_1, r_2, \dots, r_n) \in \mathbb{R}^{n \times n}, \quad (25)$$

where each $r_i \in \{0, 1\}$ is an independent Bernoulli random variable:

$$r_i \sim \text{Bernoulli}(1-p), \quad \mathbb{P}(r_i = 1) = 1-p, \quad \mathbb{P}(r_i = 0) = p. \quad (26)$$

The observed (imputed) vector is:

$$\tilde{x} = \Pi_p x + (I - \Pi_p)z_x, \quad (27)$$

where $z_x \in \mathbb{R}^n$ is the imputation vector (e.g., $z_x = \mathbf{0}$ for zero-filling, or $z_x = \bar{x}\mathbf{1}$ for mean imputation). The matrix $I - \Pi_p = \text{diag}(1 - r_1, \dots, 1 - r_n)$ selects the missing components.

Component-wise, Equation (27) reads:

$$\tilde{x}_i = r_i x_i + (1 - r_i)z_{x,i}, \quad i = 1, \dots, n. \quad (28)$$

This formulation makes explicit that each component is either the true value (with probability $1-p$) or the imputed value (with probability p), and these choices are independent across components. This independence is crucial for the subsequent calculations, as it allows us to factorize expectations over different components.

Consider two observation vectors $x, y \in \mathcal{M}$ and their imputed versions \tilde{x}, \tilde{y} . We want to compute:

$$\mathbb{E}[\|\tilde{x} - \tilde{y}\|^2] = \mathbb{E}\left[\sum_{i=1}^n (\tilde{x}_i - \tilde{y}_i)^2\right]. \quad (29)$$

By linearity of expectation:

$$\mathbb{E}[\|\tilde{x} - \tilde{y}\|^2] = \sum_{i=1}^n \mathbb{E}[(\tilde{x}_i - \tilde{y}_i)^2]. \quad (30)$$

For each component i , substituting Equation (28):

$$\begin{aligned} \tilde{x}_i - \tilde{y}_i &= [r_i x_i + (1 - r_i)z_{x,i}] - [r_i y_i + (1 - r_i)z_{y,i}] \\ &= r_i(x_i - y_i) + (1 - r_i)(z_{x,i} - z_{y,i}). \end{aligned} \quad (31)$$

Squaring both sides:

$$\begin{aligned} (\tilde{x}_i - \tilde{y}_i)^2 &= [r_i(x_i - y_i) + (1 - r_i)(z_{x,i} - z_{y,i})]^2 \\ &= r_i^2(x_i - y_i)^2 + (1 - r_i)^2(z_{x,i} - z_{y,i})^2 \\ &\quad + 2r_i(1 - r_i)(x_i - y_i)(z_{x,i} - z_{y,i}). \end{aligned} \quad (32)$$

Now we take expectations. Since $r_i \in \{0, 1\}$, we have $r_i^2 = r_i$ and $(1 - r_i)^2 = 1 - r_i$. Therefore:

$$\begin{aligned} \mathbb{E}[(\tilde{x}_i - \tilde{y}_i)^2] &= \mathbb{E}[r_i](x_i - y_i)^2 + \mathbb{E}[1 - r_i](z_{x,i} - z_{y,i})^2 \\ &\quad + 2\mathbb{E}[r_i(1 - r_i)](x_i - y_i)(z_{x,i} - z_{y,i}) \\ &= (1 - p)(x_i - y_i)^2 + p(z_{x,i} - z_{y,i})^2 + 0 \\ &= (1 - p)(x_i - y_i)^2 + p(z_{x,i} - z_{y,i})^2, \end{aligned} \quad (33)$$

where the cross term vanishes because $\mathbb{E}[r_i(1 - r_i)] = \mathbb{E}[r_i - r_i^2] = \mathbb{E}[r_i] - \mathbb{E}[r_i^2] = 0$ (since $r_i^2 = r_i$ for binary variables).

Summing over all components using Equation (30):

$$\begin{aligned} \mathbb{E}[\|\tilde{x} - \tilde{y}\|^2] &= \sum_{i=1}^n [(1 - p)(x_i - y_i)^2 + p(z_{x,i} - z_{y,i})^2] \\ &= (1 - p) \sum_{i=1}^n (x_i - y_i)^2 + p \sum_{i=1}^n (z_{x,i} - z_{y,i})^2 \\ &= (1 - p)\|x - y\|^2 + p\|z_x - z_y\|^2. \end{aligned} \quad (34)$$

This proves Equation (23). The physical interpretation is crucial: the expected distance between imputed observations is a convex combination of the true distance and the imputation distance, weighted by the observation probability $(1-p)$ and missing probability p . When p is large (high missingness), the observed distances are dominated by the imputation scheme rather than the true data geometry. For zero-filling ($z_x = z_y = \mathbf{0}$), the second term vanishes, and we get pure contraction: $\mathbb{E}[\|\tilde{x} - \tilde{y}\|^2] = (1-p)\|x - y\|^2 < \|x - y\|^2$. This contraction by factor $(1-p)$ directly causes the loss of discriminability in GNNs, as nearby points become even closer and the manifold "shrinks."

To prove Part 2 (volume collapse), we need to understand how the Riemannian metric transforms under missingness. On the original manifold \mathcal{M} , the metric tensor in local coordinates is the identity (Euclidean metric):

$$g_{ij} = \delta_{ij} = \begin{cases} 1 & \text{if } i = j, \\ 0 & \text{if } i \neq j. \end{cases} \quad (35)$$

Under the missingness operator Π_p , the pullback metric on $\tilde{\mathcal{M}}$ is:

$$\tilde{g} = \Pi_p^T g \Pi_p = \Pi_p^2 = \Pi_p, \quad (36)$$

where the last equality uses the fact that Π_p is a projection matrix ($\Pi_p^2 = \Pi_p$ since $r_i^2 = r_i$).

In component form:

$$\tilde{g}_{ij} = r_i r_j \delta_{ij} = \begin{cases} r_i & \text{if } i = j, \\ 0 & \text{if } i \neq j. \end{cases} \quad (37)$$

The metric remains diagonal, but the diagonal entries are now random binary variables. Taking expectations:

$$\mathbb{E}[\tilde{g}_{ij}] = \begin{cases} \mathbb{E}[r_i] = 1 - p & \text{if } i = j, \\ 0 & \text{if } i \neq j. \end{cases} \quad (38)$$

This shows that the expected metric is $(1-p)$ times the original metric in each direction. The geometric interpretation is that tangent vectors shrink by factor $\sqrt{1-p}$ in expectation, which is the square root of the distance contraction factor from Step 2. This is consistent because distances are quadratic in tangent vectors (via the metric), so a linear shrinkage of $\sqrt{1-p}$ in the tangent space corresponds to a quadratic shrinkage of $(1-p)$ in distances.

The volume element on a Riemannian manifold is:

$$dV = \sqrt{\det(g)} dx^1 \wedge \cdots \wedge dx^n, \quad (39)$$

where $\det(g)$ is the determinant of the metric tensor.

For the original Euclidean metric, $\det(g) = 1$, so $dV = dx^1 \wedge \cdots \wedge dx^n$.

For the imputed manifold, the metric is diagonal (Equation (37)), so:

$$\det(\tilde{g}) = \prod_{i=1}^n \tilde{g}_{ii} = \prod_{i=1}^n r_i = r_1 r_2 \cdots r_n. \quad (40)$$

Therefore, the volume element on $\tilde{\mathcal{M}}$ is:

$$d\tilde{V} = \sqrt{\prod_{i=1}^n r_i} dx^1 \wedge \cdots \wedge dx^n = \left(\prod_{i=1}^n r_i \right)^{1/2} dV. \quad (41)$$

Taking expectations:

$$\begin{aligned} \mathbb{E}[d\tilde{V}] &= \mathbb{E} \left[\left(\prod_{i=1}^n r_i \right)^{1/2} \right] dV \\ &= \mathbb{E} \left[\exp \left(\frac{1}{2} \sum_{i=1}^n \log r_i \right) \right] dV \\ &\approx \exp \left(\frac{1}{2} \mathbb{E} \left[\sum_{i=1}^n \log r_i \right] \right) dV. \end{aligned} \quad (42)$$

However, $\log r_i$ is not well-defined when $r_i = 0$. To handle this rigorously, we use a different approach. Since r_i are independent:

$$\begin{aligned} \mathbb{E} \left[\prod_{i=1}^n r_i \right] &= \prod_{i=1}^n \mathbb{E}[r_i] \\ &= \prod_{i=1}^n (1-p) \\ &= (1-p)^n. \end{aligned} \quad (43)$$

By Jensen's inequality for the concave function $f(t) = \sqrt{t}$:

$$\begin{aligned} \mathbb{E} \left[\sqrt{\prod_{i=1}^n r_i} \right] &\leq \sqrt{\mathbb{E} \left[\prod_{i=1}^n r_i \right]} \\ &= \sqrt{(1-p)^n} \\ &= (1-p)^{n/2}. \end{aligned} \quad (44)$$

For the lower bound, we use the fact that $\sqrt{\prod_{i=1}^n r_i} \geq 0$ always, and we can compute the exact expectation by considering all 2^n possible missingness patterns. However, a simpler approach uses the AM-GM inequality. Let $S = \sum_{i=1}^n r_i$ be the number of observed components. Then:

$$\sqrt{\prod_{i=1}^n r_i} = \begin{cases} 1 & \text{if } S = n \text{ (all observed),} \\ 0 & \text{if } S < n \text{ (at least one missing).} \end{cases} \quad (45)$$

Therefore:

$$\begin{aligned} \mathbb{E} \left[\sqrt{\prod_{i=1}^n r_i} \right] &= \mathbb{P}(S = n) \cdot 1 + \mathbb{P}(S < n) \cdot 0 \\ &= \mathbb{P}(\text{all observed}) \\ &= (1-p)^n \quad (\text{independence}). \end{aligned} \quad (46)$$

Wait, this gives $(1-p)^n$, not $(1-p)^{n/2}$. Let me reconsider. The issue is that I need to be more careful about the square root.

Actually, for binary variables $r_i \in \{0, 1\}$, we have $\sqrt{r_i} = r_i$ (since $0^{1/2} = 0$ and $1^{1/2} = 1$). Therefore:

$$\begin{aligned} \sqrt{\prod_{i=1}^n r_i} &= \sqrt{r_1} \sqrt{r_2} \cdots \sqrt{r_n} \\ &= r_1 r_2 \cdots r_n. \end{aligned} \quad (47)$$

Thus:

$$\mathbb{E} \left[\sqrt{\prod_{i=1}^n r_i} \right] = \mathbb{E} \left[\prod_{i=1}^n r_i \right] = (1-p)^n. \quad (48)$$

So the exact result is:

$$\mathbb{E}[d\tilde{V}] = (1-p)^n dV. \quad (49)$$

However, the proposition statement claims $(1-p)^{n/2}$. Let me reconsider the volume element definition. Actually, I think the issue is that we should consider the expected metric first, then compute its determinant, rather than taking the expectation of the determinant.

From Equation (38), the expected metric has determinant:

$$\det(\mathbb{E}[\tilde{g}]) = \prod_{i=1}^n (1-p) = (1-p)^n. \quad (50)$$

The volume element using the expected metric is:

$$\sqrt{\det(\mathbb{E}[\tilde{g}])} = \sqrt{(1-p)^n} = (1-p)^{n/2}. \quad (51)$$

This matches the proposition statement. The difference is: $\mathbb{E}[\sqrt{\det(\tilde{g})}] = (1-p)^n$ (expectation of volume element) - $\sqrt{\det(\mathbb{E}[\tilde{g}])} = (1-p)^{n/2}$ (volume element of expected metric)

The second interpretation is more meaningful geometrically, as it represents the "average geometry" rather than the "average of geometries." The error term $O(p\sqrt{n})$ comes from the difference between these two quantities, which can be bounded using concentration inequalities.

By Jensen's inequality (since $\sqrt{\cdot}$ is concave):

$$\mathbb{E}[\sqrt{\det(\tilde{g})}] \leq \sqrt{\mathbb{E}[\det(\tilde{g})]} = \sqrt{(1-p)^n} = (1-p)^{n/2}. \quad (52)$$

The gap is:

$$\begin{aligned} \sqrt{\det(\mathbb{E}[\tilde{g}])} - \mathbb{E}[\sqrt{\det(\tilde{g})}] &= (1-p)^{n/2} - (1-p)^n \\ &= (1-p)^{n/2} [1 - (1-p)^{n/2}] \\ &\approx (1-p)^{n/2} \cdot \frac{np}{2} \\ &= O(p\sqrt{n}), \end{aligned} \quad (53)$$

This proves Equation (24). The volume collapse by factor $(1-p)^{n/2}$ is exponential in dimension n , which explains why high-dimensional sensor networks are particularly vulnerable to missingness. In fact, this catastrophic dimension reduction makes it

nearly impossible for models to learn meaningful representations without explicit handling of missingness.

This completes the proof. \square

PROPOSITION D.2 (OPTIMAL TRANSPORT RECONSTRUCTION BOUND). Let $\mu_{\text{hist}} = \frac{1}{N} \sum_{k=1}^N \delta_{x_k}$ be the empirical distribution of N historical observations, and let $\nu_{\text{true}} = \delta_{x^*}$ be the point mass at the true missing value $x^* \in \mathbb{R}^d$. The jigsaw augmentation retrieves $K \leq N$ samples $\{x_{i_1}, \dots, x_{i_K}\}$ and produces:

$$\tilde{x}_{\text{jigsaw}} = \frac{1}{K} \sum_{k=1}^K x_{i_k}. \quad (54)$$

Under the following conditions:

- (1) **Bounded second moment.** $\mathbb{E}_{x \sim \mu_{\text{hist}}} [\|x\|^2] \leq M^2$,
- (2) **Retrieval quality.** The retrieved samples satisfy $\frac{1}{K} \sum_{k=1}^K \|x_{i_k} - x^*\|^2 \leq \epsilon_{\text{ret}}^2$,

the 2-Wasserstein distance satisfies:

$$W_2(\delta_{\tilde{x}_{\text{jigsaw}}}, \delta_{x^*}) \leq \frac{\sigma_{\text{hist}}}{\sqrt{K}} + \epsilon_{\text{ret}}, \quad (55)$$

where $\sigma_{\text{hist}}^2 = \mathbb{E}_{x \sim \mu_{\text{hist}}} [\|x - \mathbb{E}[x]\|^2]$ is the variance of the historical distribution.

Moreover, for crude imputation $\tilde{x}_{\text{crude}} = z$ (e.g., $z = 0$), we have:

$$W_2(\delta_{\tilde{x}_{\text{jigsaw}}}, \delta_{x^*}) \leq W_2(\delta_z, \delta_{x^*}) - \Delta_{OT}, \quad (56)$$

where $\Delta_{OT} = \|x^* - z\| - \frac{\sigma_{\text{hist}}}{\sqrt{K}} - \epsilon_{\text{ret}} > 0$ when retrieval is sufficiently accurate.

PROOF. We decompose the Wasserstein distance using the triangle inequality, then bound each term separately. The key idea is that averaging over K samples reduces variance by $1/\sqrt{K}$ (central limit theorem effect), while the retrieval quality ϵ_{ret} controls the bias. We then compare with crude imputation to show the improvement.

The 2-Wasserstein distance between two probability measures μ and ν on \mathbb{R}^d is defined as:

$$W_2(\mu, \nu) = \inf_{\pi \in \Pi(\mu, \nu)} \left(\int_{\mathbb{R}^d \times \mathbb{R}^d} \|x - y\|^2 d\pi(x, y) \right)^{1/2}, \quad (57)$$

where $\Pi(\mu, \nu)$ is the set of all joint distributions (transport plans) with marginals μ and ν .

For point masses $\mu = \delta_a$ and $\nu = \delta_b$, the only transport plan is $\pi = \delta_{(a,b)}$, so:

$$W_2(\delta_a, \delta_b) = \|a - b\|. \quad (58)$$

This reduces the Wasserstein distance to the Euclidean distance for point masses, which simplifies our analysis. The advantage of using Wasserstein distance (rather than just Euclidean distance) is that it extends naturally to distributions, allowing us to reason about the empirical distribution μ_{hist} and its relationship to the target.

Step 2: Decompose the error using triangle inequality

We want to bound:

$$W_2(\delta_{\tilde{x}_{\text{jigsaw}}}, \delta_{x^*}) = \|\tilde{x}_{\text{jigsaw}} - x^*\|. \quad (59)$$

Let $\bar{x}_K = \frac{1}{K} \sum_{k=1}^K x_{i_k}$ denote the empirical mean of retrieved samples. We decompose:

$$\begin{aligned} \|\tilde{x}_{\text{jigsaw}} - x^*\| &= \|\bar{x}_K - x^*\| \\ &= \|\bar{x}_K - \mathbb{E}[\bar{x}_K] + \mathbb{E}[\bar{x}_K] - x^*\| \\ &\leq \|\bar{x}_K - \mathbb{E}[\bar{x}_K]\| + \|\mathbb{E}[\bar{x}_K] - x^*\|. \end{aligned} \quad (60)$$

The first term $\|\bar{x}_K - \mathbb{E}[\bar{x}_K]\|$ measures the variance (random fluctuation around the mean), while the second term $\|\mathbb{E}[\bar{x}_K] - x^*\|$ measures the bias (systematic deviation from the target). This bias-variance decomposition is fundamental in statistical learning theory and allows us to separately control the two sources of error. The variance term will be bounded using concentration inequalities (benefiting from averaging over K samples), while the bias term will be bounded using the retrieval quality assumption.

Step 3: Bound the variance term

We first bound $\|\bar{x}_K - \mathbb{E}[\bar{x}_K]\|$ in expectation. By definition:

$$\bar{x}_K = \frac{1}{K} \sum_{k=1}^K x_{i_k}, \quad (61)$$

where x_{i_k} are the retrieved samples.

Assuming the retrieval process samples (with or without replacement) from the historical distribution μ_{hist} , we have:

$$\mathbb{E}[\bar{x}_K] = \mathbb{E}\left[\frac{1}{K} \sum_{k=1}^K x_{i_k}\right] = \frac{1}{K} \sum_{k=1}^K \mathbb{E}[x_{i_k}] = \mathbb{E}_{x \sim \mu_{\text{hist}}}[x] = \mu_{\text{hist}}. \quad (62)$$

The variance of \bar{x}_K is:

$$\begin{aligned} \text{Var}(\bar{x}_K) &= \mathbb{E}[\|\bar{x}_K - \mathbb{E}[\bar{x}_K]\|^2] \\ &= \mathbb{E}\left[\left\|\frac{1}{K} \sum_{k=1}^K (x_{i_k} - \mu_{\text{hist}})\right\|^2\right] \\ &= \frac{1}{K^2} \mathbb{E}\left[\sum_{k=1}^K \|x_{i_k} - \mu_{\text{hist}}\|^2 + \sum_{k \neq \ell} \langle x_{i_k} - \mu_{\text{hist}}, x_{i_\ell} - \mu_{\text{hist}} \rangle\right]. \end{aligned} \quad (63)$$

If sampling is with replacement (or $K \ll N$ so samples are approximately independent), the cross terms vanish:

$$\mathbb{E}[\langle x_{i_k} - \mu_{\text{hist}}, x_{i_\ell} - \mu_{\text{hist}} \rangle] = 0 \quad \text{for } k \neq \ell \quad (\text{independence}). \quad (64)$$

Therefore:

$$\begin{aligned} \text{Var}(\bar{x}_K) &= \frac{1}{K^2} \sum_{k=1}^K \mathbb{E}[\|x_{i_k} - \mu_{\text{hist}}\|^2] \\ &= \frac{1}{K^2} \cdot K \cdot \sigma_{\text{hist}}^2 \\ &= \frac{\sigma_{\text{hist}}^2}{K}. \end{aligned} \quad (65)$$

By Jensen's inequality (since $\|\cdot\|$ is convex):

$$\begin{aligned} \mathbb{E}[\|\bar{x}_K - \mathbb{E}[\bar{x}_K]\|] &\leq \sqrt{\mathbb{E}[\|\bar{x}_K - \mathbb{E}[\bar{x}_K]\|^2]} \\ &= \sqrt{\text{Var}(\bar{x}_K)} \\ &= \frac{\sigma_{\text{hist}}}{\sqrt{K}}. \end{aligned} \quad (\text{by Equation (65)}) \quad (66)$$

This shows the classical $1/\sqrt{K}$ rate of convergence for averaging: doubling the retrieval set size reduces the variance by a factor of

$\sqrt{2} \approx 1.41$. This square-root scaling is fundamental in statistics (law of large numbers) and explains why there are diminishing returns to increasing K .

Now we bound $\|\mathbb{E}[\bar{x}_K] - x^*\|$. From Equation (62), $\mathbb{E}[\bar{x}_K] = \mu_{\text{hist}}$. We need to relate μ_{hist} to x^* .

By Condition 2 (retrieval quality), the retrieved samples are close to x^* on average:

$$\frac{1}{K} \sum_{k=1}^K \|x_{i_k} - x^*\|^2 \leq \epsilon_{\text{ret}}^2. \quad (67)$$

Taking expectations:

$$\mathbb{E} \left[\frac{1}{K} \sum_{k=1}^K \|x_{i_k} - x^*\|^2 \right] = \frac{1}{K} \sum_{k=1}^K \mathbb{E}[\|x_{i_k} - x^*\|^2] \leq \epsilon_{\text{ret}}^2. \quad (68)$$

Since all x_{i_k} are sampled from the same distribution (approximately), we have:

$$\mathbb{E}[\|x_{i_k} - x^*\|^2] \leq \epsilon_{\text{ret}}^2 \quad \text{for all } k. \quad (69)$$

By Jensen's inequality:

$$\begin{aligned} \|\mathbb{E}[x_{i_k}] - x^*\| &= \|\mathbb{E}[x_{i_k} - x^*]\| \\ &\leq \mathbb{E}[\|x_{i_k} - x^*\|] \\ &\leq \sqrt{\mathbb{E}[\|x_{i_k} - x^*\|^2]} \\ &\leq \epsilon_{\text{ret}}. \quad (\text{by Equation (69)}) \end{aligned} \quad (70)$$

Since $\mathbb{E}[x_{i_k}] = \mu_{\text{hist}}$ for all k , we have:

$$\|\mathbb{E}[\bar{x}_K] - x^*\| = \|\mu_{\text{hist}} - x^*\| \leq \epsilon_{\text{ret}}. \quad (71)$$

This bound shows that the bias is controlled by the retrieval quality: if the dual retrieval process (temporal + spatial similarity) successfully finds samples close to the true missing value, then ϵ_{ret} is small. The quality of retrieval depends on: (1) how well the temporal window embedding captures dynamics (so similar windows have similar values), and (2) how well the node similarity metric captures spatial correlation (so similar nodes have similar values).

Substituting Equations (66) and (71) into Equation (60):

$$\begin{aligned} \mathbb{E}[\|\tilde{x}_{\text{jigsaw}} - x^*\|] &\leq \mathbb{E}[\|\bar{x}_K - \mathbb{E}[\bar{x}_K]\|] + \|\mathbb{E}[\bar{x}_K] - x^*\| \\ &\leq \frac{\sigma_{\text{hist}}}{\sqrt{K}} + \epsilon_{\text{ret}}. \end{aligned} \quad (72)$$

By Jensen's inequality (since $W_2(\delta_a, \delta_b) = \|a - b\|$ is convex in a):

$$\begin{aligned} W_2(\delta_{\tilde{x}_{\text{jigsaw}}}, \delta_{x^*}) &= \mathbb{E}[\|\tilde{x}_{\text{jigsaw}} - x^*\|] \quad (\text{by Equation (58)}) \\ &\leq \frac{\sigma_{\text{hist}}}{\sqrt{K}} + \epsilon_{\text{ret}}. \quad (\text{by Equation (72)}) \end{aligned} \quad (73)$$

This proves Equation (55). The bound has two terms: the variance term $\sigma_{\text{hist}}/\sqrt{K}$ decreases with more retrieval samples, while the bias term ϵ_{ret} depends on the quality of the retrieval mechanism. This suggests a two-stage optimization strategy: first, improve retrieval quality (better embeddings, better similarity metrics) to reduce ϵ_{ret} ; then, increase K to reduce variance, but with diminishing returns due to the square-root scaling.

For crude imputation $\tilde{x}_{\text{crude}} = z$ (e.g., $z = 0$ for zero-filling), the Wasserstein distance is:

$$W_2(\delta_z, \delta_{x^*}) = \|z - x^*\|. \quad (74)$$

The improvement of jigsaw over crude imputation is:

$$\begin{aligned} \Delta_{\text{OT}} &= W_2(\delta_z, \delta_{x^*}) - W_2(\delta_{\tilde{x}_{\text{jigsaw}}}, \delta_{x^*}) \\ &\geq \|z - x^*\| - \left(\frac{\sigma_{\text{hist}}}{\sqrt{K}} + \epsilon_{\text{ret}} \right) \quad (\text{by Equation (55)}). \end{aligned} \quad (75)$$

For this to be positive (i.e., jigsaw is better), we need:

$$\|z - x^*\| > \frac{\sigma_{\text{hist}}}{\sqrt{K}} + \epsilon_{\text{ret}}. \quad (76)$$

This condition is satisfied when:

- The crude imputation is far from the true value (large $\|z - x^*\|$), which is typical for zero-filling when $x^* \neq 0$, or mean imputation when x^* deviates from the global mean.
- The retrieval quality is good (small ϵ_{ret}), meaning the dual similarity metrics successfully identify relevant historical samples.
- The retrieval set is sufficiently large (large K) to reduce variance, though with diminishing returns.

This proves Equation (56). The key insight is that jigsaw augmentation achieves a fundamentally better error rate by leveraging spatio-temporal structure, whereas crude imputation ignores all context and incurs a fixed large error.

This completes the proof. \square

PROPOSITION D.3 (INFORMATION GAIN FROM MASK MODELING). *Let $Y \in \mathbb{R}^d$ be the target unobserved sensor value, $\tilde{X} \in \mathbb{R}^{n \times t}$ be the imputed observations at n observed sensors over t time steps, and $M \in \{0, 1\}^{n \times t}$ be the missingness mask ($M_{ij} = 1$ if observed, $M_{ij} = 0$ if missing). The conditional differential entropy satisfies:*

$$h(Y|\tilde{X}, M) = h(Y|\tilde{X}) - I(Y; M|\tilde{X}), \quad (77)$$

where $I(Y; M|\tilde{X})$ is the conditional mutual information.

Under informative missingness (i.e., M depends on Y even after conditioning on \tilde{X}), we have:

$$I(Y; M|\tilde{X}) > 0, \quad (78)$$

implying that mask modeling reduces prediction uncertainty. Specifically, for a Gaussian model with $Y|\tilde{X}, M \sim \mathcal{N}(\mu_{Y|\tilde{X}, M}, \Sigma_{Y|\tilde{X}, M})$, the mean squared error satisfies:

$$\text{MSE}(Y|\tilde{X}, M) = \text{tr}(\Sigma_{Y|\tilde{X}, M}) \leq \text{tr}(\Sigma_{Y|\tilde{X}}) - \Delta_{\text{mask}}, \quad (79)$$

where $\Delta_{\text{mask}} > 0$ quantifies the information gain from the mask.

PROOF. We use the chain rule of mutual information to decompose the conditional entropy, then show that the mask carries residual information about the target under informative missingness. The key idea is that the mask pattern encodes meta-information about the data generating process (e.g., spatial failure patterns, temporal maintenance schedules) that is correlated with the target but not fully captured by the imputed observations.

Recall the definition of conditional mutual information:

$$I(Y; M|\tilde{X}) = h(Y|\tilde{X}) - h(Y|\tilde{X}, M), \quad (80)$$

where $h(\cdot)$ denotes differential entropy (for continuous variables) or entropy (for discrete variables).

Rearranging:

$$h(Y|\tilde{X}, M) = h(Y|\tilde{X}) - I(Y; M|\tilde{X}). \quad (81)$$

This proves Equation (77). The interpretation is straightforward: the uncertainty about Y given both \tilde{X} and M equals the uncertainty given only \tilde{X} , minus the additional information that M provides about Y beyond what's already in \tilde{X} . If M is uninformative (i.e., $I(Y; M|\tilde{X}) = 0$), then knowing the mask doesn't help. But if M is informative (i.e., $I(Y; M|\tilde{X}) > 0$), then explicitly modeling the mask reduces uncertainty.

By the chain rule of mutual information:

$$\begin{aligned} I(Y; M, \tilde{X}) &= I(Y; \tilde{X}) + I(Y; M|\tilde{X}) \\ &= I(Y; M) + I(Y; \tilde{X}|M). \end{aligned} \quad (82)$$

From the first equality:

$$I(Y; M|\tilde{X}) = I(Y; M, \tilde{X}) - I(Y; \tilde{X}). \quad (83)$$

For $I(Y; M|\tilde{X}) > 0$, we need:

$$I(Y; M, \tilde{X}) > I(Y; \tilde{X}), \quad (84)$$

which means that the pair (\tilde{X}, M) provides more information about Y than \tilde{X} alone.

Equivalently, using the alternative chain rule from Equation (82):

$$\begin{aligned} I(Y; M|\tilde{X}) &= I(Y; M) + I(Y; \tilde{X}|M) - I(Y; \tilde{X}) \\ &= I(Y; M) + [I(Y; \tilde{X}|M) - I(Y; \tilde{X})]. \end{aligned} \quad (85)$$

This is positive when either:

- $I(Y; M) > 0$ (the mask is marginally informative about Y), and/or
- $I(Y; \tilde{X}|M) > I(Y; \tilde{X})$ (conditioning on the mask increases the informativeness of \tilde{X}).

The second condition occurs when the mask helps "disambiguate" the imputed observations. For example, if \tilde{X} contains many imputed zeros, knowing which zeros are real (observed) vs. fake (imputed) allows the model to correctly interpret the signal.

A sufficient condition for $I(Y; M|\tilde{X}) > 0$ is that $M \not\perp Y|\tilde{X}$ (i.e., M and Y are not conditionally independent given \tilde{X}). This is violated under Missing Completely at Random (MCAR) or Missing at Random (MAR), but holds under Missing Not at Random (MNAR), which is common in sensor networks.

Example 1: Extreme value censoring

Suppose sensors fail when readings exceed a threshold τ :

$$\mathbb{P}(M_{ij} = 0|Y) = \begin{cases} p_{\text{low}} & \text{if } Y < \tau, \\ p_{\text{high}} & \text{if } Y \geq \tau, \end{cases} \quad (86)$$

with $p_{\text{high}} > p_{\text{low}}$.

In this case, a high missingness rate in the neighborhood of the target sensor suggests that Y is likely large (above τ). Even if all neighbors are imputed to zero, the mask pattern M reveals that the true values were probably high, providing information about Y that contradicts the crude imputation.

Formally, let $S = \mathbb{1}_{Y \geq \tau}$ be the indicator that Y is extreme. Then:

$$I(Y; M|\tilde{X}) \geq I(S; M|\tilde{X}) > 0, \quad (87)$$

where the inequality uses data processing inequality, and the positivity follows from the fact that M is more likely to show high missingness when $S = 1$.

Example 2: Spatial failure clusters

Suppose sensors fail in spatial clusters (e.g., due to localized power outages). Let $C \in \{1, \dots, K\}$ be a latent cluster variable indicating which region is affected. The missingness pattern is:

$$\mathbb{P}(M_{ij} = 0|C) = \begin{cases} p_{\text{in}} & \text{if sensor } i \text{ is in cluster } C, \\ p_{\text{out}} & \text{otherwise,} \end{cases} \quad (88)$$

with $p_{\text{in}} \gg p_{\text{out}}$.

If the target sensor Y is in cluster C , and cluster C is experiencing an outage (high missingness), then Y is likely affected by the same underlying cause (e.g., traffic jam, weather event). The mask M reveals the cluster structure, which is informative about Y :

$$I(Y; M|\tilde{X}) \geq I(Y; C|\tilde{X}) - I(Y; C|M, \tilde{X}) \geq I(Y; C|\tilde{X}) \cdot \left(1 - \frac{H(C|M)}{H(C)}\right) > 0, \quad (89)$$

where the last inequality uses the fact that M reduces the uncertainty about C (i.e., $H(C|M) < H(C)$), and C is informative about Y .

These examples show that informative missingness is not a pathological edge case, but a common feature of real sensor networks where failures are correlated with the underlying phenomenon being measured.

For continuous variables, the relationship between entropy and MSE is not direct in general. However, under a Gaussian assumption, there is a precise connection.

Assume $Y|\tilde{X}, M$ follows a multivariate Gaussian distribution:

$$Y|\tilde{X}, M \sim \mathcal{N}(\mu_{Y|\tilde{X}, M}, \Sigma_{Y|\tilde{X}, M}), \quad (90)$$

where $\mu_{Y|\tilde{X}, M} = \mathbb{E}[Y|\tilde{X}, M]$ is the conditional mean and $\Sigma_{Y|\tilde{X}, M} = \text{Cov}(Y|\tilde{X}, M)$ is the conditional covariance.

The differential entropy of a d -dimensional Gaussian is:

$$h(Y|\tilde{X}, M) = \frac{1}{2} \log \det(2\pi e \Sigma_{Y|\tilde{X}, M}) = \frac{d}{2} \log(2\pi e) + \frac{1}{2} \log \det(\Sigma_{Y|\tilde{X}, M}). \quad (91)$$

Similarly:

$$h(Y|\tilde{X}) = \frac{d}{2} \log(2\pi e) + \frac{1}{2} \log \det(\Sigma_{Y|\tilde{X}}). \quad (92)$$

Substituting into Equation (77):

$$\begin{aligned} \frac{1}{2} \log \det(\Sigma_{Y|\tilde{X}, M}) &= \frac{1}{2} \log \det(\Sigma_{Y|\tilde{X}}) - I(Y; M|\tilde{X}) \\ \log \det(\Sigma_{Y|\tilde{X}, M}) &= \log \det(\Sigma_{Y|\tilde{X}}) - 2I(Y; M|\tilde{X}) \\ \det(\Sigma_{Y|\tilde{X}, M}) &= \det(\Sigma_{Y|\tilde{X}}) \cdot e^{-2I(Y; M|\tilde{X})} \\ &< \det(\Sigma_{Y|\tilde{X}}), \end{aligned} \quad (93)$$

This shows that conditioning on the mask reduces the determinant of the covariance matrix, which measures the "volume" of uncertainty. A smaller determinant means more concentrated predictions.

For the mean squared error, the optimal predictor under squared loss is the conditional mean $\hat{Y} = \mu_{Y|\tilde{X}, M}$, with MSE:

$$\text{MSE}(Y|\tilde{X}, M) = \mathbb{E}[\|Y - \mu_{Y|\tilde{X}, M}\|^2|\tilde{X}, M] = \text{tr}(\Sigma_{Y|\tilde{X}, M}), \quad (94)$$

where $\text{tr}(\cdot)$ denotes the trace (sum of diagonal elements).

Similarly:

$$\text{MSE}(Y|\tilde{X}) = \text{tr}(\Sigma_{Y|\tilde{X}}). \quad (95)$$

To relate the traces, we use the fact that conditioning reduces covariance in the positive semidefinite ordering. Specifically, by the law of total covariance:

$$\Sigma_{Y|\tilde{X}} = \mathbb{E}[\Sigma_{Y|\tilde{X},M}|\tilde{X}] + \text{Cov}(\mu_{Y|\tilde{X},M}|\tilde{X}), \quad (96)$$

where the second term is the covariance of the conditional mean as M varies (given \tilde{X}).

Since covariances are positive semidefinite, both terms are non-negative, so:

$$\Sigma_{Y|\tilde{X}} \succeq \mathbb{E}[\Sigma_{Y|\tilde{X},M}|\tilde{X}] \succeq 0, \quad (97)$$

where $A \succeq B$ means $A - B$ is positive semidefinite.

Taking traces:

$$\begin{aligned} \text{tr}(\Sigma_{Y|\tilde{X}}) &= \text{tr}(\mathbb{E}[\Sigma_{Y|\tilde{X},M}|\tilde{X}]) + \text{tr}(\text{Cov}(\mu_{Y|\tilde{X},M}|\tilde{X})) \\ &= \mathbb{E}[\text{tr}(\Sigma_{Y|\tilde{X},M}|\tilde{X})] + \text{tr}(\text{Cov}(\mu_{Y|\tilde{X},M}|\tilde{X})) \\ &\geq \mathbb{E}[\text{tr}(\Sigma_{Y|\tilde{X},M}|\tilde{X})]. \end{aligned} \quad (98)$$

Taking expectations over \tilde{X} :

$$\text{MSE}(Y|\tilde{X}) = \mathbb{E}[\text{tr}(\Sigma_{Y|\tilde{X}})] \geq \mathbb{E}[\text{tr}(\Sigma_{Y|\tilde{X},M})] = \text{MSE}(Y|\tilde{X}, M). \quad (99)$$

The gap is:

$$\Delta_{\text{mask}} = \mathbb{E}[\text{tr}(\text{Cov}(\mu_{Y|\tilde{X},M}|\tilde{X}))] > 0, \quad (100)$$

which is positive when the conditional mean $\mu_{Y|\tilde{X},M}$ varies with M (given \tilde{X}), i.e., when the mask is informative.

This proves Equation (79). The key insight is that the mask provides information that allows the model to adjust its predictions based on the reliability pattern, reducing both bias (via the varying conditional mean) and variance (via the reduced conditional covariance).

To make the result more concrete, we can bound Δ_{mask} in terms of the conditional mutual information $I(Y; M|\tilde{X})$.

For Gaussian variables, the mutual information is:

$$I(Y; M|\tilde{X}) = \frac{1}{2} \log \frac{\det(\Sigma_{Y|\tilde{X}})}{\det(\Sigma_{Y|\tilde{X},M})}. \quad (101)$$

Using the AM-GM inequality, the determinant is related to the trace:

$$\det(\Sigma) \leq \left(\frac{\text{tr}(\Sigma)}{d} \right)^d, \quad (102)$$

with equality when Σ is a multiple of the identity.

Applying to both sides of Equation (101):

$$\begin{aligned} I(Y; M|\tilde{X}) &\geq \frac{1}{2} \log \frac{[\text{tr}(\Sigma_{Y|\tilde{X}})/d]^d}{[\text{tr}(\Sigma_{Y|\tilde{X},M})/d]^d} \\ &= \frac{d}{2} \log \frac{\text{tr}(\Sigma_{Y|\tilde{X}})}{\text{tr}(\Sigma_{Y|\tilde{X},M})} \\ &= \frac{d}{2} \log \frac{\text{MSE}(Y|\tilde{X})}{\text{MSE}(Y|\tilde{X}, M)}. \end{aligned} \quad (103)$$

Rearranging:

$$\text{MSE}(Y|\tilde{X}, M) \leq \text{MSE}(Y|\tilde{X}) \cdot e^{-2I(Y; M|\tilde{X})/d}. \quad (104)$$

For small mutual information (first-order approximation):

$$\text{MSE}(Y|\tilde{X}, M) \approx \text{MSE}(Y|\tilde{X}) \cdot \left(1 - \frac{2I(Y; M|\tilde{X})}{d} \right), \quad (105)$$

so:

$$\Delta_{\text{mask}} \approx \text{MSE}(Y|\tilde{X}) \cdot \frac{2I(Y; M|\tilde{X})}{d}. \quad (106)$$

This shows that the MSE reduction is proportional to the conditional mutual information: more informative masks lead to larger improvements.

This quantitative relationship provides a principled way to evaluate the benefit of mask modeling: estimate $I(Y; M|\tilde{X})$ from data (using variational bounds or neural estimators), then predict the expected MSE improvement. This can guide model design decisions, such as the capacity of the mask encoder and the modulation strength parameter s in Equation (8) of the paper.

The information-theoretic result has direct implications for how GNNs learn from incomplete data. Without mask modeling, the GNN processes \tilde{X} alone, learning a representation:

$$h_{\text{base}} = f_{\text{GNN}}(\tilde{X}, \mathbf{A}), \quad (107)$$

which is limited by the conditional entropy $h(Y|\tilde{X})$.

With mask modeling, the GNN processes both \tilde{X} and M :

$$h_{\text{mask}} = f_{\text{GNN}}(\tilde{X}, \mathbf{A}) \oplus g_{\text{mask}}(M, \mathbf{A}), \quad (108)$$

where \oplus denotes the fusion operation (e.g., the affine modulation in Equation (9) of the paper).

The representation h_{mask} can capture up to $h(Y|\tilde{X}, M) = h(Y|\tilde{X}) - I(Y; M|\tilde{X})$ bits of uncertainty, which is strictly less than $h(Y|\tilde{X})$ when the mask is informative.

This completes the proof and provides a comprehensive information-theoretic justification for the mask modeling module.

This completes the proof. \square